Optics and Lasers in Engineering 176 (2024) 108075

Contents lists available at ScienceDirect

Optics and Lasers in Engineering

journal homepage: www.elsevier.com/locate/optlaseng

The SOLUS instrument: Optical characterization of the first hand-held probe for multimodal imaging (ultrasound and multi-wavelength time-resolved diffuse optical tomography)

Giulia Maffeis [a,*], Laura Di Sieno [a], Alberto Dalla Mora [a], Antonio Pifferi [a,i], Alberto Tosi [b], Enrico Conca [b], Andrea Giudice [c], Alessandro Ruggeri [c], Simone Tisa [c], Alexander Flocke [d], Bogdan Rosinski [e], Jean-Marc Dinten [f], Mathieu Perriollat [f], Jonathan Lavaud [g], Simon Arridge [h], Giuseppe Di Sciacca [h], Andrea Farina [i], Pietro Panizza [j], Elena Venturini [j], Peter Gordebeke [k], Paola Taroni [a,i]

[a] Politecnico di Milano, Dipartimento di Fisica, Piazza Leonardo da Vinci 32, 20133 Milano, Italy
[b] Politecnico di Milano, Dipartimento di Elettronica, Informazione e Bioingegneria, Piazza Leonardo da Vinci 32, 20133 Milano, Italy
[c] Micro Photon Devices Srl, Via Waltraud Gebert Deeg 3f, 39100 Bolzano, Italy
[d] iC-Haus, Am Kuemmerling 18, 55294 Bodenheim, Germany
[e] Vermon S.A., 67 rue Fromentel, 37000 Tours, France
[f] CEA-LETI, 17 Avenue des Martyrs, 38054 Grenoble, France
[g] Hologic Supersonic Imagine S.A., 135 rue Emilien Gautier, 13290 Aix en Provence, France
[h] University College London, Department of Computer Science, Gower Street WC1E 6BT London, UK
[i] Consiglio Nazionale delle Ricerche, Istituto di Fotonica e Nanotecnologie, Piazza Leonardo da Vinci 32, 20133 Milano, Italy
[j] Scientific Institute (IRCCS) Ospedale San Raffaele-Breast Imaging Unit, Via Olgettina 60, 20132 Milano, Italy
[k] European Institute for Biomedical Imaging Research, Am Gestade 1, 1010 Vienna, Austria

ARTICLE INFO

Keywords:
SOLUS
Miniaturized diffuse optical system
Time-resolved near-infrared spectroscopy
Diffuse optical tomography
Multimodal hand-held probe
Breast lesion diagnosis

ABSTRACT

SOLUS is a multimodal imaging system comprising the first miniaturized handheld device to perform time domain Diffuse Optical Tomography at 8 visible and near infrared wavelengths. The hand-held probe also includes B-mode ultrasounds, Shear Wave Elastography and Color Doppler sonography, being its first goal the multiparametric non-invasive diagnosis of breast cancer. This work aims at presenting the system and its main capabilities, focusing on the optical characterization carried out to assess the overall performance of the developed photonics technologies (picosecond pulsed lasers, high-sensitive time-gated sensors and integrated electronics) and of the software for tomographic reconstructions (perturbative model based on Born approximation).

Systematic measurements performed on tissue-mimicking phantoms, reproducing a perturbation (e.g., a lesion) in a homogenous background, helped understand the system efficiency range. Variations in absorption are tracked with acceptable quality, which is key to estimate tissue composition, up to 0.25 cm^{-1} for the bulk (relative error on average of 16 %) and 0.16 cm^{-1} for sufficiently big perturbations (relative error on average of 26 % for 6 cm^3 inhomogeneities). Instead, the system showed low sensitivity to a localized perturbation in scattering and a relative error on average of 17 % for the scattering bulk assessment. An example case of clinical measurement is also discussed.

1. Introduction

In 2020, breast cancer became the most diffused neoplasia worldwide. Among women, it accounts for 24.5 % of cancer cases and 15.5 % of cancer deaths [1]. Medical imaging is the primary and least invasive tool to detect and characterize breast cancer, by providing information about morphology or physiology of tissues, depending on the specific technique [2,3]. However, current imaging techniques have relevant

* Corresponding author.
E-mail address: giulia.maffeis@polimi.it (G. Maffeis).

https://doi.org/10.1016/j.optlaseng.2024.108075
Received 22 September 2023; Received in revised form 19 January 2024; Accepted 25 January 2024
Available online 16 February 2024

limitations: X-ray mammography shows low sensitivity on dense breasts and involves the use of ionizing radiation, the interpretation of ultrasounds images depends on the operator experience, while Magnetic Resonance Imaging and Positron Emission Tomography are characterized by high costs and long examination time [2,3].

Also, studies brought out that mammographic screening programs are fundamental to reduce breast cancer mortality, but have a significant 50–60 % rate of false positive mammograms on a 10-year period [4–6]. This leads to unnecessary invasive procedures (typically biopsy), with the consequent discomfort to the patients and waste of financial resources.

Thus, there is a clear need for new non-invasive tools to characterize breast cancer. In this framework, diffuse optical breast imaging has already been presented as a promising technique [7–11]. At the same time, a multimodal approach, focusing on different aspects of tissue characterization, could increase the overall potential.

The SOLUS project (Smart OpticaL and UltraSound diagnostics of breast cancer) is indeed devoted to the design, development and testing in laboratory and clinics of a multimodal hand-held probe for breast imaging, aimed at the non-invasive discrimination between malignant and benign breast lesions. It proposes the integration of time-resolved multi-wavelength Diffuse Optical Tomography (DOT) and ultrasound-based imaging techniques (B-mode ultrasounds—US, Color Doppler imaging—CD, Shear Wave Elastography—SWE) into a unique hand-held probe [12–14]. The combination of new photonics and more standard imaging modalities aims at a comprehensive quantitative characterization of breast lesions, based on composition (hemoglobin, water, lipids and collagen concentrations through DOT), morphologic information (US), functional blood features (CD) and mechanical parameters (e.g., stiffness, through SWE).

Miniaturized picosecond pulsed lasers and high-sensitive time-gated detectors are the break-through elements of the SOLUS optical basic module, the “optode” [15]. Combined with a commercial US transducer, the optode enabled the implementation of the multimodal hand-held probe.

SOLUS multimodality does not materialize only as a posteriori cross-correlation among DOT and ultrasounds-based findings, but also via the extrapolation of morphological priors to enhance the performance of the DOT system [16,17]. In fact, a well-known shortcoming of diffuse optical imaging is its limited spatial resolution, due to the highly diffusive nature of light in biological tissues in the red and infrared spectral range. The exploitation of a priori anatomical constraints obtained through B-mode, X-ray or MRI images already led to a distinctly more accurate quantification of the optical properties, and in turn of tissue composition, with respect to DOT data alone, thus improving the diagnostic potential of the technique [18–27].

This paper aims at presenting the hardware and software of the SOLUS system and an initial performance assessment in laboratory prior to the clinical study. After a detailed description of the setup and measurement settings (Section 2) and of the data analysis methods (Section 3), the outcomes of the ultrasound transducer assessment (Section 4) and of the validation of the SOLUS multimodal probe on phantoms are reported (Section 5). Finally, an example of multimodal in vivo measurement is presented in Section 6.

2. Experimental setup

The implementation of the first ever miniaturization of multi-wavelength time-resolved DOT in a hand-held probe was made possible by the development of the optode, a stand-alone module to perform time domain (TD) multi-wavelength diffuse optical spectroscopy.

In this Section, we describe the optode components (Section 2.1) and the integration of eight optodes in the multimodal probe (Section 2.2), which was conceived as part of a high-end commercial ultrasonography system (Section 2.3), the Aixplorer Mach 30 from Hologic SuperSonic Imaging [28,29]. Section 2.4 describes the software able to run a measurement and Section 2.5 the problems encountered while testing the prototype. Finally, Section 2.6 describes the measurement procedure.

Fig. 1. The SOLUS multimodal system (left) and a zoom on the hand-held probe (right). The US transducer is located in central position, sided by the optodes.

2.1. The optode

A SOLUS optode is a compact module (2.3 × 1.2 × 1.4 cm^3) containing [15]:

- eight pulsed laser diodes emitting at 640, 675, 830, 905, 930, 970, 1020, and 1050 nm, each driven by 4 dual picosecond laser pulser integrated circuits;
- a fast-gated digital Silicon PhotoMultiplier (dSiPM), with programmable active area composed of 1728 pixels (8.6 mm^2);
- an integrated Time-to-Digital Converter (TDC) to implement Time Correlated Single Photon Counting (TCSPC);
- control and power electronics.

Fast-gating helps improve the sensitivity to absorption by investigating the output pulse at different time windows. SPADs are turned ON and OFF repeatedly so as to divide the output Distribution Of Time-of-Flight (DTOF) into slices [30,31]. Each acquisition occurs at a fixed optimized count rate by dynamically increasing the number of active pixels (i.e., low number for early gates close to the pulse peak, high number for late gates in correspondence of the pulse tail). Therefore, after proper normalization to the active area, the slices can be interlaced post-processing via software to generate a new gated curve with a much higher dynamic range. The amplitude gain can reach 3–4 decades, thus enhancing the sensitivity to deep tissue optical properties [32]. The first gated acquisition can be considered equivalent to a free-running acquisition (i.e., standard acquisition, without fast-gating), provided that the gate width is sufficiently large (3–4 ns).

2.2. The SOLUS probe

The SOLUS multimodal probe encompasses a regular ultrasound transducer for B-mode US, CD and SWE (256 elements 50 mm-large linear array with a central frequency around 7 MHz, Hologic SuperSonic Imagine S.A., France [29]), sided by eight optodes (four on each side, Fig. 1).

Table 1
Scheme of the source (S) –detector (D) distances. It displays the high symmetry of the probe, considering eight unique values. Distances are calculated between the centres of the S and the D and are expressed in centimetres.

	S1	S2	S3	S4	S5	S6	S7	S8
D1	0.67	1.46	2.68	3.96	2.83	3.11	3.84	4.82
D2	1.46	0.67	1.46	2.68	3.11	2.83	3.11	3.84
D3	2.68	1.46	0.67	1.46	3.84	3.11	2.83	3.11
D4	3.96	2.68	1.46	0.67	4.82	3.84	3.11	2.83
D5	2.83	3.11	3.84	4.82	0.67	1.46	2.68	3.96
D6	3.11	2.83	3.11	3.84	1.46	0.67	1.46	2.68
D7	3.84	3.11	2.83	3.11	2.68	1.46	0.67	1.46
D8	4.82	3.84	3.11	2.83	3.96	2.68	1.46	0.67

Table 2
Power of the lasers available in each source of the SOLUS probe. Values expressed in milliwatt.

λ [nm]	S1	S2	S3	S4	S5	S6	S7	S8
640	1.44	1.24	1.42	1.43	1.75	1.43	1.75	1.72
675	3.25	2.79	2.7	1.27	1.98	2.49	2.44	2
830	0.95	0.73	0.85	0.83	1.09	0.98	0.93	0.77
905	4.38	3.39	2.73	2.2	3.82	2.93	2.81	3.31
930	2.63	2.07	2.11	2.21	2.6	2.19	2.45	3.02
970	1.79	0.98	0.89	1.06	1.77	1.62	1.72	2.13
1020	2.42	1.86	1.91	1.89	2.36	2.23	2.39	2.39
1050	1.8	0.8	1.8	1.25	2.14	2.52	1.99	2.35

Each module (i.e., each optode) lays on a printed circuit board mounted orthogonally to the corresponding front-end window. A prism properly conveys the signal from the sample to the chip. The optode window is covered by a long-pass filter (Schott OG590) to minimize stray light. For the same reason, the lasers and the detector windows are physically separated. The probe footprint is 80 mm × 55 mm, a compromise between maximized technological compactness and ease of handling for the operator. Table 1 reports the source-detector distances relative to all source-detector couples, while Table 2 the power of the 64 lasers.

The probe is provided with five terminals:

- the cable for US, which is connected to the main body of the Aixplorer Mach 30 (Section 2.3);
- input and output pipes for the water-cooling system (EXT-440CU Computer Liquid Cooling System, Rev3.0, Koolance, USA), which warrants temperature control and correct operation of the probe detector and electronics;
- the cable for DOT, which is connected to a power injector and a PC, in this order. Indeed, the ultrasonography system has been adapted to host a computer (Intel® Core™ i7–8700T CPU @ 2.40 GHz) and a touch screen to manage the whole measurement procedure (left screen in Fig. 1).
- the cable for the position sensor, which keeps track of the probe movements during measurements.

Finally, an isolating transformer (1000 VA A-50, REOMED GmbH, Germany) guarantees safe use of electrical equipment in a medical environment in agreement with relevant regulations.

It is important to underline that the multimodal probe can be used limited to optical acquisitions even connected to a PC, separately from the ultrasonography system.

2.3. The ultrasonography system

The cart-based SuperSonic Ultrasound Mach 30 system is used to perform non-invasive diagnostic general purpose ultrasound imaging procedures.

It allows the operator to run measurements, capture images and review the results in the form of a report. It provides a wide variety of information thanks to a large panel of imaging modes: anatomical (B-mode) and functional (M-mode, Color Doppler, Angio P.L.U.S, Pulsed Wave Doppler, Continuous Wave Doppler). Moreover, it allows to access tissue elasticity maps through ShearWave™ elastography. The modalities involved in the SOLUS protocol are limited to B-mode, Color Doppler and SWE.

2.4. The SOLUS system software

The SOLUS software, encoded in MatLab with a modular structure, implements the following core functionalities:

- frontend for the hardware drivers (communication with SuperSonic Ultrasound Mach 30, initialization of smart optodes and position sensor);

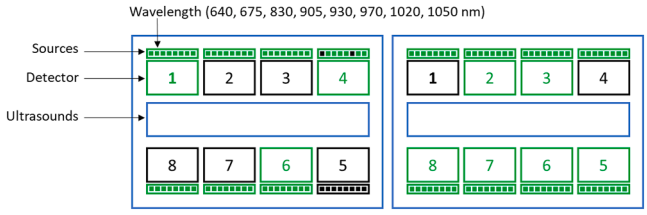

Fig. 2. Schematic representation of the SOLUS probe (shown in Fig. 1, right). In each optode, the big window represents the detector, the small window represents the array of sources and each single filled square a single source at a certain wavelength. The schematic is used to depict the current status of the first (left) and second (right) SOLUS probes: green color highlights active optical elements.

- control of the measurement procedure performing optical and US data acquisitions (e.g., selection of acquisition sequence and settings, visualization of DTOFs during measurement);
- processing of optical signal, implementing and displaying DOT reconstructions;
- collection of the patients' information during clinical tests;
- management and storage of database, including experimental data and metadata.

These functionalities are managed through a user interface, designed for the operator who pilots the machine and performs the clinical examination.

2.5. Hardware challenges

As explained previously, the SOLUS multimodal probes are cutting-edge prototypes that include unprecedented photonics technologies. Their complete fabrication, assembly and test required several travels from one partner to another. Besides, like any medical instrumentation, they have been subject to thorough and extensive electrical, ultrasound and water-tightness tests prior to laboratory and clinical characterization.

Such intense operations, interventions and movements could be the cause of the sudden hardware damage limited to optical parts encountered on the first SOLUS probe when delivered to Politecnico di Milano for the validation in laboratory (March 2021). Similar (even though more limited) damage occurred later on (March 2022) with the second probe, despite the particular attention paid during fabrication, being us aware of the previous experience. Therefore, both SOLUS probes are not fully operative. Their current status is depicted in Fig. 2.

Nevertheless, it is worth mentioning that the SOLUS probe provides redundant information due to its highly symmetric disposition of sources and detectors. Also, despite the partial functionality, the results of the characterization on phantoms described in the following are consistent with the ones obtained during a similar procedure performed prior to hardware problems. Therefore, the probes have been considered suitable for laboratory and clinical validation. The performance assessment has been carried out with the second probe, and Table 2 refers to the second probe as well.

2.6. The measurement procedure

2.6.1. DOT acquisition

An efficient optical measurement requires three kinds of acquisitions:

- *Preliminary light trimming*: fine tuning of the collected light intensity to reach a specific count rate target (in this case, $10^5 \frac{photons}{s} \times 0.01\ s = 10^3\ photons$ for each acquisition) by activating a certain number of pixels in each detector.

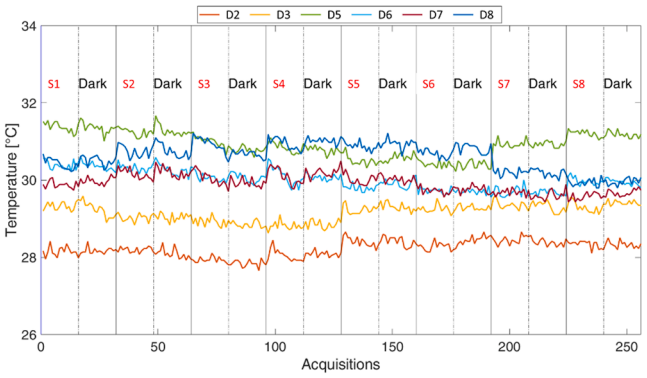

Fig. 3. Temperature throughout acquisitions at 1050 nm, separately for each detector. "S" stands for source and "D" for detector. The following number identifies the optode.

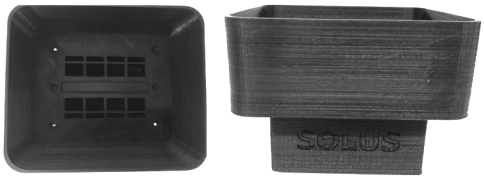

Fig. 4. Top (left) and front (right) view of the SOLUS IRF box.

- *Acquisition on the sample*: real measurement performed with the active area defined at the previous step.
- *Instrument Response Function (IRF)*: acquisition (after proper light trimming as well) in order to evaluate the setup non-idealities, enabling to decouple the effects of the instrument from the sample features on pulses.

During an optical acquisition, sources emit sequentially, while detection takes place simultaneously over the available sensors. Any acquisition including light injection is always followed by an identical acquisition (with the same active area per each gate) without shining lasers to estimate the background noise, thus permitting to remove it from the former measurement.

Fig. 3 shows how temperature keeps quite stable throughout the measurement, never exceeding 32 °C, thanks to the cooling system (29.81 °C ± 0.99 °C on average over detectors temporal mean values). Similar results are obtained for the other wavelengths.

2.6.2. IRF for optical acquisitions

In diffuse optical measurements the acquisition of the IRF is essential for an accurate reconstruction of the tissue optical properties.

Ideally, the IRF should be acquired by placing face-to-face sources and detectors to remove any intermediate medium and distance.

However, this strategy is not feasible for the SOLUS probe. In this case, the solution adopted was the use of a tailored 3D printed "IRF box" (black PLA filament, 3DiTALY, shown in Fig. 4) [33]. The probe is placed into a housing, whose back end is provided with a mask that reproduces the probe optodes arrangement. The housing is attached to a 2.5-cm-deep box. Therefore, performing a standard optical measurement, light goes through the source windows of the housing, propagates into the box diffusely reflecting on its floor and walls, and travels back to the probe, by crossing the detector windows. This implies that light propagates in air along certain optical paths, that delay the output pulses, depending on the source-detector distance and the depth of the box. Such delays must be evaluated and properly compensated for an accurate convolution with the theoretical model.

Different approaches exist to estimate such delays. The current strategy consists in computing them based on geometrical considerations: the time required to travel along the shortest path from source to detector with a single reflection on the box floor.

It is important to underline that, although the IRF box method seemed the best alternative, it still might introduce errors since it prevents the knowledge of the exact optical paths travelled by photons inside the box, which is fundamental for high accuracy. The method explained above allows only an approximate estimation of delays, thus the IRF may significantly influence the quality of the final results.

2.6.3. Multimodal acquisition

Multimodal measurements imply the involvement of the US transducer and, consequently, of the ultrasonographic system. The four kinds of acquisitions (B-mode, CD, SWE, DOT) are performed sequentially.

In vivo measurements are carried out setting the sound speed to 1480 m/s (value optimized for breast tissue), while it needs to be reduced to 1020 m/s to properly distinguish structures on the Ecoflex silicone phantoms fabricated for the SOLUS characterization (Section 5.1).

As for a regular US examination, the contact between the probe and the patient's skin or phantom surface needs to be mediated by a gel to minimize the effects of material mismatch. Different brands were considered and, after systematic optical tests, the choice fell on the Parker Laboratories Polysonic Ultrasound Lotion (Parker Laboratories, INC., USA): it is white, sufficiently diffusive to avoid light short circuits between source and detector, and at the same time has moderate viscosity to prevent signal distortion [34].

2.6.4. Measurement protocol

The SOLUS examination consists in evaluating B-mode US, CD, SWE and DOT on 4 different positions while the subject lies supine lifting the arm ipsilateral to measured breast. Initially, the radiologist localizes the lesion with a standard (commercial) US probe. Then, he/she places the SOLUS probe aligned with the direction of the maximum lesion diameter (position 1) and starts the examination, acquiring a B-mode image, a Color Doppler image and a shear wave elastography with the US transducer available in the SOLUS probe (same as the one of the commercial probe). Finally DOT measurements are performed through the optodes. The sequence is then repeated along the orthogonal axis at the lesion location (position 2), in the healthy breast tissue far from the lesion (ipsi-control measurement, position 3), and in the mirror location of the contralateral breast (contra-control measurement, position 4). Control measurements are required to assess the contrast between the healthy and the lesion tissues, whereas the evaluation of structures from different perspectives is a diffused radiological approach to improve accuracy in diagnosis.

At the end of each series of acquisitions on the lesion (positions 1 and 2), the operator marks the lesion contours on the B-mode images displayed on the touch screen of the SOLUS system. This is the segmentation procedure required for US-guided DOT (Section 3.2). The full protocol is repeated by 3 radiologists in order to assess operator independence.

Once US and optical data are collected and the segmentation has been accomplished, an online (i.e., real-time, in about 5 min) US-guided DOT reconstruction is performed to obtain a preliminary tissue composition and microstructure assessment and check the adequacy of the measurement, directly with the PC mounted on the system. However, in-depth data analysis for diagnostic purposes is carried out offline, after the measurement, with another PC (Intel® Xeon® CPU E5-2650 v3 @ 2.30 GHz). The entire SOLUS examination usually requires one hour.

The measurement routine for the phantom characterization has been designed to mimic the SOLUS clinical protocol. In fact, two measurements on the heterogeneity and two measurements on the homogeneous background along orthogonal axes are taken. Here, B-mode images are used only as morphological prior for DOT, while CD and SWE are neglected.

3. Methods for optical data analysis

After proper pre-processing, a tomographic model for media embedding a heterogeneity is applied to the SOLUS optical data. In the following, we illustrate the main details of each stage. Also, a homogeneous model is used to fit measurements acquired on media devoid of a heterogeneity.

3.1. DTOF pre-processing

Prior to DOT reconstruction, curves undergo a series of pre-processing algorithms to compensate for, in this order:

- *Counts loss*: the TDC cannot accept any new photon when busy converting previous data. Such photon loss can be compensated a posteriori for an efficient matching of the acquired pulse slices.
- *Differential non-linearity*: the time bins width of the TDC are not perfectly uniform, thus distorting the resulting DTOF. They can be re-equalized a posteriori, granting a fair estimation of optical properties.
- *Noise contribution*: the noise DTOF is always subtracted from the corresponding sample DTOF to remove the contribution of both dark counts and stray light.
- *Saturation recognition*: an algorithm based on empirical findings is applied and saturated curves are discarded. This happens almost systematically for the shortest source-detector distance (0.67 cm), where injection and collection occur in the same optode and light intensity attains indeed the highest value. However, as a rule of thumb, in reflectance geometry, the depth reached by photons is half of the source-detector distance. Then, its exclusion affects only the assessment of a very superficial layer of the medium.

After these steps, the resulting DTOFs can undergo an extra pre-processing step involving wide dynamic range DTOF reconstruction in case of fast-gated acquisitions [32] or be directly analyzed using the models described in the next Sections, for a free-running approach employing first gate curves.

However, in this paper we will present only preliminary results, focusing on the system basic performance. Therefore, we discuss outcomes based on the use of the first gate DTOFs (equivalent to a free running acquisition). The study of reconstructed gated curves is part of future work.

3.2. 3D extrapolation from US-based lesion segmentation

Since B-mode images are bidimensional, the extrapolation to obtain a 3D mask is essential to match the volumetric distribution of DOT. In brief, the extrusion of the binary mask into the third dimension can be performed by applying a snake-based method [35], starting from user-defined control points (i.e., lesion segmentation). A cubic spline interpolation approximates the border of the lesion, then an extrapolation method based on the distance transform is responsible for the generation of the 3D volume [16].

3.3. Heterogeneous model for DOT

The DTOFs resulting from the pre-processing stage are analyzed applying the Born Approximation for time-resolved reflectance measurements on a semi-infinite medium, embedding a perturbation.

The analytical curves (64 source-detector distances for 8 wavelengths, each one distributed over 128 time bins, ranging from 74.9 to 89.4 ps each, depending on the detector in the second probe) are convolved with the corresponding IRF to take into account the setup non-idealities. An acquisition on the perturbation is always coupled with an acquisition on a homogeneous portion of the medium to estimate contrasts. The localization of the perturbation is guided by the morphological constraint provided by the 3D extrapolation of the US segmentation. The enforcement of the US prior is related to the regularization parameter τ in the tomographic approach. The stronger the regularization, the stronger the smoothing effect (decreasing noise). However, this happens at the expenses of accuracy, which reduces as τ increases [36]. The final tomography encloses $29 \times 30 \times 31$ cubic voxels, each with a 2-mm side.

These procedures are encoded in the software for DOT summarized in the next Section. The description is limited to a condensed presentation of the model, defining the main quantities involved. It does not make explicit otherwise significant conditions and requirements for the sake of brevity [16,17].

3.4. The tomographic approach

DOT seeks to reconstruct the 3D spatial distribution of the probed tissue optical properties voxel by voxel from the collected DTOFs. In the case of a spectrally constrained approach [37], aimed at retrieving the constituents' concentrations ($C_{k,0}$) and the scattering parameters (a_0,b_0), this can be described by the following linearized inverse problem:

$$\begin{aligned}\delta\Phi_a\left(\vec{r}_d,t,\lambda\right) &= J_a\left(\vec{r}_s,\vec{r},\vec{r}_d,t,C_{k,0},a_0,b_0\right)\delta\mu_a(\vec{r},\lambda),\\ \delta\Phi_D\left(\vec{r}_d,t,\lambda\right) &= J_D\left(\vec{r}_s,\vec{r},\vec{r}_d,t,C_{k,0},a_0,b_0\right)\delta D(\vec{r},\lambda),\end{aligned} \tag{1}$$

All involved parameters are defined and described below, from Eqs. (2) to (7). The number of output variables reduces from 7 (i.e., oxy- and deoxy-hemoglobin, water, lipid, collagen, a—amplitude - and b—slope - scattering parameters) to 2 when a standard fit, addressed to quantify μ_a and $\mu_s' = \frac{1}{3D}$ (D is the diffusion coefficient), is applied. In this case, Eq. (3), that incorporates the Lambert-Beer law (relating absorption coefficients and constituents' concentrations) and the Mie empirical model (relating scattering coefficients and amplitude and slope parameters), must not be replaced.

The DOT inverse problem is intrinsically ill-posed, and, together with the linearization due to the Born approximation, an additional possible strategy to improve robustness is the exploitation of structural priors (encoded in $\tau\mathscr{R}([\delta C_k(\vec{r});\delta a(\vec{r}),\delta b(\vec{r})])$) deriving from US images. The resulting problem is:

$$\begin{aligned}[\delta C_k(\vec{r});\delta a(\vec{r}),\delta b(\vec{r})] = \underset{\delta C_k,\delta a,\delta b}{argmin}\Bigg\{&\sum_i\left(\frac{\phi_i(t)-J_S\left(\vec{r}_s,\vec{r},\vec{r}_d,t,C_{k,0},a_0,b_0,\lambda\right)\left[\delta C_k\left(\vec{r}_s,\vec{r},\vec{r}_d,t\right);\delta a\left(\vec{r}_s,\vec{r},\vec{r}_d,t\right),\delta b\left(\vec{r}_s,\vec{r},\vec{r}_d,t\right)\right]}{\sigma_i}\right)^2\\ &+\tau\mathscr{R}\left(\left[\delta C_k\left(\vec{r}_s,\vec{r},\vec{r}_d,t\right);\delta a\left(\vec{r}_s,\vec{r},\vec{r}_d,t\right),\delta b\left(\vec{r}_s,\vec{r},\vec{r}_d,t\right)\right]\right)\Bigg\},\end{aligned} \tag{2}$$

Here a list of the quantities involved in Eq. (1):

- λ: wavelength,
- t: time,
- $\vec{r}$: position of the voxel,
- $\vec{r}_s$: position of the source,
- $\vec{r}_d$: position of the detector,
- $\mu_{a,0}$ and D_0: background absorption and diffusion coefficients,
- $\delta\mu_a(\vec{r}_s, \vec{r}, \vec{r}_d, t)$ and $\delta D(\vec{r}_s, \vec{r}, \vec{r}_d, t)$: space-dependent variations in absorption and diffusion coefficients due to the heterogeneity,

$$\delta\mu_a(\vec{r},\lambda) = \sum_k \int_k (\lambda)\delta C_k(\vec{r}),$$
$$\delta D(\vec{r},\lambda) = \left[-\frac{1}{3a_0^2}\left(\frac{\lambda_0}{\lambda}\right)^{-b_0}\right]\delta a(\vec{r}) + \left[-\frac{1}{3a_0}\left(\frac{\lambda_0}{\lambda}\right)^{-b_0}\ln\left(\frac{\lambda_0}{\lambda}\right)\right]\delta b(\vec{r}). \tag{3}$$

- J_a and J_D: absorption and scattering sensitivity matrices, also known as Jacobians,
- ϵ_k: extinction coefficient of the kth constituent,
- $C_{k,0}, a_0, b_0$: background concentrations of the k breast constituents and scattering parameters,
- $[\delta C_k(\vec{r}_s, \vec{r}, \vec{r}_d, t); \delta a(\vec{r}_s, \vec{r}, \vec{r}_d, t), \delta b(\vec{r}_s, \vec{r}, \vec{r}_d, t)]$: corresponding variations in each voxel due to the heterogeneity, With reference to Eq. (2):
- $\phi_i(t) = (\Phi_{pert}(t) - \Phi_{bkg}(t))_i$: fluence variation measured at the points corresponding to the SOLUS optodes due to the heterogeneity, normalized in area, for each source-detector couple i;
- J_S: Jacobian matrix for each source-detector distance i (r_i), deriving from the linearization of the spectral model due to the Born approximation, as expressed in Eqs. (4)–(6);

$$\begin{aligned} J_S(r_i, \vec{r}, t, C_{k,0}, a_0, b_0, \lambda) = {} & J_a(r_i, \vec{r}, t, C_{k,0}, a_0, b_0)\sum_k \epsilon_k(\lambda)\delta C_k(\vec{r}) \\ & + J_{D,a}(r_i, \vec{r}, t, C_{k,0}, a_0, b_0, \lambda)\delta a(\vec{r}) \\ & + J_{D,b}(r_i, \vec{r}, t, C_{k,0}, a_0, b_0, \lambda)\delta b(\vec{r}), \end{aligned} \tag{4}$$

$$J_{D,a}\left(\vec{r}_s, \vec{r}, \vec{r}_d, t, C_{k,0}, a_0, b_0, \lambda\right) = J_D\left(\vec{r}_s, \vec{r}, \vec{r}_d, t, C_{k,0}, a_0, b_0\right)\left[-\frac{1}{3a_0^2}\left(\frac{\lambda_0}{\lambda}\right)^{-b_0}\right], \tag{5}$$

$$J_{D,b}\left(\vec{r}_s, \vec{r}, \vec{r}_d, t, C_{k,0}, a_0, b_0, \lambda\right) = J_D\left(\vec{r}_s, \vec{r}, \vec{r}_d, t, C_{k,0}, a_0, b_0\right)\left[-\frac{1}{3a_0}\left(\frac{\lambda_0}{\lambda}\right)^{-b_0}\ln\left(\frac{\lambda_0}{\lambda}\right)\right]. \tag{6}$$

- $\sigma_i^2 = \frac{\phi_i(t)}{\sum_{k=1}^{N_{tw}}\int_{T_k}^{T_{k+1}}\phi_{i,NN}(t)}$: standard deviation of self-normalized signal with Poisson distribution; T_k refers to a specific time bin, N_{tw} is the total number of time bins, $\phi_{i,NN}(t)$ is the original, not normalized signal;
- $\mathscr{R}([\delta C_k(\vec{r}); \delta a(\vec{r}), \delta b(\vec{r})])$: regularization expression that plays the role of a penalty term;
- τ: regularization parameter.

The heart of US-guided DOT is the regularization, that exploits geometrical constraints to improve the reconstruction and smooth image artefacts:

$$\begin{aligned} \mathscr{R}([\delta C_k(\vec{r}); \delta a(\vec{r}), \delta b(\vec{r})]) = {} & \| K(\vec{r})\nabla\delta C_{k,0}(\vec{r})\|^2 + \| K(\vec{r})\nabla\delta a_0(\vec{r})\|^2 \\ & + \| K(\vec{r})\nabla\delta b_0(\vec{r})\|^2. \end{aligned} \tag{7}$$

This is done by integrating the 3D extrapolation of the lesion segmentation (encoding its position, shape and size), contained in the quantity $K(\vec{r})$. In homogeneous regions, the regularization is intense and has a smoothing effect, whereas in the presence of edges the regularization is softer, so as to preserve structures.

This procedure leads to 3D images for chromophore concentrations and scattering parameters that correctly localize the lesion and modulate the contrast between lesion and healthy tissue composition.

The reconstruction procedure requires about 5 min with the first SOLUS probe and 12 min with the second, using a PC with the following processor: Intel® Xeon® CPU E5-2650 v3 @ 2.30 GHz. The DOT procedure for a complete set of optical paths (i.e., a fully operative probe) would require about 20 min.

3.5. Homogeneous analytical model

The analytical solution to the diffusion equation for a homogeneous semi-infinite medium, obtained using the extrapolated boundary condition in reflectance geometry is [38]:

$$R(\rho,t) = \frac{e^{\left[\frac{\rho^2}{4Dvt}\right]}e^{-\mu_a vt}}{2(4\pi Dv)^{\frac{3}{2}}t^{\frac{5}{2}}}\left[z_{r-}e^{\left[-\frac{z_{r-}^2}{4Dvt}\right]} - z_{r+}e^{\left[-\frac{z_{r+}^2}{4Dvt}\right]}\right] \tag{8}$$

with

$$\begin{cases} z_{r-} = -z_s \\ z_{r+} = 2z_e + z_s \end{cases} \tag{9}$$

and ρ is the source-detector distance, z_s the depth of a Dirac delta source $q_0(\vec{r},t) = \delta^3(\vec{r} - \vec{r}_s)\delta(t)$ placed at $\vec{r}_s = (0,0,z_s)$ and z_e the extrapolated distance.

4. Ultrasound characterization

Despite being based on the commercial Superlinear™ L18_5 probe, previously validated by Hologic SuperSonic Imaging and Vermon S.A., the addition of optical components in the SOLUS probe required the application of technical and safety tests to comply respectively with the declared specifications and the clinical use.

The technical test passed correctly: all ultrasound elements are functional and exhibit a central frequency at 7 MHz with 128 % of relative bandwidth and an excellent sensitivity.

As regard the clinical use, according to IEC 60601-2-37 standard [39], electrical, acoustical and thermal safety criteria were evaluated, involving all the imaging modes considered in the SOLUS project. The HiPot test (1500 V) and 260 VAC test ensured that the probe is safe of electrical shocks, with a leakage current of only 12 μA. Furthermore, the acoustic output and surface probe temperature are compliant with the

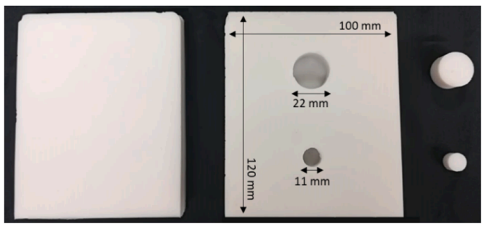

Fig. 5. A SOLUS phantom kit.

standards limits. Therefore, the US transducer does not represent any risk for the patient or the operator.

5. Optical characterization on phantoms

The characterization on phantoms aims at testing the SOLUS probe under controlled conditions, prior to the in vivo assessment. The characterization focus is the optical performance, while the use of B-mode images is limited to the heterogeneity localization, when present.

In the following, the preliminary results of the characterization will be illustrated, after a description of the phantoms design and of the measurement scheme.

5.1. Phantom design

5.1.1. SOLUS phantom kit

Custom-made bi-modal phantoms with tissue-mimicking optical and ultrasound properties were fabricated specifically for the SOLUS system [40]. The goal was to reproduce the geometry of a breast embedding a lesion, that can be studied in reflectance geometry (as the clinical protocol foresees patients to be in supine position).

The chosen materials for heterogeneous phantoms are Ecoflex (00-30, Smooth-On, Inc. PA, USA) and Sylgard (S184, Dow Corning Corp. CA, USA), two kinds of silicone that manifest an echogenic contrast (i.e., Sylgard appears darker than Ecoflex at US).

A phantom kit (Fig. 5) is composed of:

- a bulk ($12 \times 10 \times 4$ cm^3) with two cylindrical cavities (1 cm^3 and 6 cm^3);
- two movable cylindrical heterogeneities (here called also inclusions);

Table 3
Conventionally true values for absorption coefficients (cm^{-1}) of phantoms (Ecoflex) and inclusions (Sylgard) at the eight wavelengths. The first 2 columns report the label properties.

	μ_s' [cm^{-1}]	μ_a [cm^{-1}]	Wavelength [nm]							
			640	675	830	905	930	970	1020	1050
SYLGARD	**6**	**0.08**	0.086	0.085	0.085	0.230	0.089	0.088	0.146	0.095
	12	**0.04**	0.042	0.040	0.038	0.165	0.040	0.039	0.089	0.045
		0.08	0.086	0.083	0.081	0.212	0.084	0.083	0.135	0.087
		0.16	0.133	0.130	0.128	0.262	0.130	0.128	0.183	0.135
		0.32	0.259	0.254	0.254	0.393	0.256	0.255	0.306	0.259
		0.48	0.388	0.382	0.381	0.526	0.381	0.381	0.436	0.387
	18	**0.08**	0.095	0.091	0.086	0.208	0.086	0.084	0.134	0.089
ECOFLEX	**6**	**0.08**	0.092	0.086	0.086	0.244	0.090	0.093	0.155	0.099
	12	**0.04**	0.053	0.049	0.046	0.188	0.049	0.048	0.104	0.051
		0.08	0.097	0.091	0.089	0.236	0.090	0.092	0.149	0.096
		0.16	0.190	0.177	0.171	0.324	0.175	0.178	0.233	0.178
	18	**0.08**	0.096	0.089	0.086	0.222	0.086	0.089	0.142	0.091

Table 4
Conventionally true values for reduced scattering coefficients (cm^{-1}) of phantoms (Ecoflex) and inclusions (Sylgard) at the 8 wavelengths. The first 2 columns report the label properties.

	μ_s' [cm^{-1}]	μ_a [cm^{-1}]	Wavelength [nm]							
			640	675	830	905	930	970	1020	1050
SYLGARD	**6**	**0.08**	6.03	5.74	4.21	3.86	3.48	3.18	2.99	2.77
	12	**0.04**	11.90	11.17	8.38	7.11	6.94	6.44	5.86	5.65
		0.08	12.07	11.28	8.42	7.29	7.02	6.55	6.01	5.69
		0.16	11.82	11.07	8.35	7.33	7.00	6.45	6.08	5.72
		0.32	12.84	12.09	9.19	8.26	7.73	7.24	6.67	6.34
		0.48	11.96	11.32	8.70	7.87	7.32	6.89	6.43	6.16
	18	**0.08**	20.02	18.77	13.95	11.73	11.53	10.66	9.68	9.27
	6	**0.08**	7.00	6.49	4.63	4.12	3.78	3.42	3.22	2.88
ECOFLEX	**12**	**0.04**	14.34	13.47	9.93	8.32	8.12	7.44	6.78	6.33
		0.08	12.71	11.71	8.53	7.35	6.93	6.36	5.89	5.50
		0.16	12.12	11.28	8.29	7.30	6.85	6.41	5.91	5.48
	18	**0.08**	19.94	18.75	13.77	11.51	11.31	10.46	9.56	9.06

Table 5
Conventionally true values for absorption and reduced scattering coefficients of MEDPHOT homogeneous phantoms (resin) at the eight wavelengths. Values in cm^{-1}.

	[cm^{-1}]	Wavelength [nm]							
		640	675	830	905	930	970	1020	1050
μ_a	**0.05 (B2)**	0.061	0.056	0.048	0.102	0.077	0.088	0.109	0.102
	0.15 (B4)	0.176	0.165	0.138	0.178	0.152	0.158	0.176	0.168
	0.25 (B6)	0.292	0.274	0.228	0.254	0.227	0.228	0.244	0.233
	0.35 (B8)	0.407	0.383	0.318	0.329	0.302	0.298	0.311	0.298
μ'_s	**10 (All)**	8.51	7.63	5.28	4.52	4.30	3.99	3.65	3.46

Table 6
List of measurements performed for the characterization on phantoms.

ID	Inclusion size [cm^3]	$\mu_{s,\ bulk}^{'}$ [cm^{-1}]	$\mu_{a,\ bulk}$ [cm^{-1}]	$\mu_{s,\ incl}^{'}$ [cm^{-1}]	$\mu_{a,\ incl}$ [cm^{-1}]	Material
1	6	12	0.08	12	0.04	Silicone
2	6	12	0.08	12	0.08	Silicone
3	6	12	0.08	12	0.16	Silicone
4	6	12	0.08	12	0.32	Silicone
5	6	12	0.08	12	0.48	Silicone
6	1	12	0.08	12	0.04	Silicone
7	1	12	0.08	12	0.08	Silicone
8	1	12	0.08	12	0.16	Silicone
9	1	12	0.08	12	0.32	Silicone
10	1	12	0.08	12	0.48	Silicone
11	6	12	0.08	6	0.08	Silicone
12	6	12	0.08	18	0.08	Silicone
13	1	12	0.08	6	0.08	Silicone
14	1	12	0.08	18	0.08	Silicone
15	6	6	0.08	12	0.08	Silicone
16	6	18	0.08	12	0.08	Silicone
17	6	12	0.04	12	0.08	Silicone
18	6	12	0.16	12	0.08	Silicone
19	–	10	0.05	–	–	Resin
20	–	10	0.15	–	–	Resin
21	–	10	0.25	–	–	Resin
22	–	10	0.35	–	–	Resin

- a top layer (0.5 × 12 × 10 cm^3).

All the elements of a kit are characterized by the same well-defined optical properties (μ_a and $\mu_s^{'}$) and are made of Ecoflex, except for the inclusions. In fact, two kinds of inclusion exist: Ecoflex inclusions are used to match the bulk properties and reproduce an optical and US homogeneous medium, whereas Sylgard inclusions mimic the effect of a heterogeneity (breast lesion).

Five phantom kits of different reduced scattering and absorption properties (6 cm^{-1}–0.08 cm^{-1}, 12 cm^{-1}–0.04 cm^{-1}, 12 cm^{-1}–0.08 cm^{-1}, 12 cm^{-1}–0.16 cm^{-1}, 18 cm^{-1}–0.08 cm^{-1}) and seven Sylgard inclusions, combining five absorption (0.04, 0.08, 0.16, 0.32, 0.48 cm^{-1}) and three reduced scattering coefficients (6, 12, 18 cm^{-1}) have been fabricated. Each element is shortly referred to as the rounded optical properties at about 690 nm. We will refer to these values as "label properties".

The optical properties of phantoms and inclusions at the SOLUS wavelengths (Tables 3 and 4) were measured with a state-of-the-art Diffuse Optical Spectroscopy system in optimal operating conditions [41], and here are considered as the conventionally true values for the estimation of errors.

5.1.2. MEDPHOT phantom kit

We also evaluated the linearity of the system to different bulk absorption coefficients using homogenous phantoms. This is useful for the assessment of the average breast parenchyma composition. For this purpose, we used a set of well-characterized phantoms in resin, part of the MEDPHOT kit [42]. The B series, corresponding to a nominal $\mu_s^{'} = 10$ cm^{-1}, can be considered comparable to the $\mu_s^{'} = 12$ cm^{-1} SOLUS phantoms. The advantage is the availability of absorption levels up to 0.35 cm^{-1} rather than 0.16 cm^{-1} (B2, B4, B6, B8, as shown in Table 5).

Resin is not suitable for US investigation, but in this case the absence of an inclusion makes this detail irrelevant.

5.2. Dataset

The characterization on phantoms summarized in Table 6 and reported in the following was performed with the second SOLUS probe.

The investigated parameters are the system sensitivity to:

- the inclusion absorption coefficient ($\mu_{a,\ incl}$),

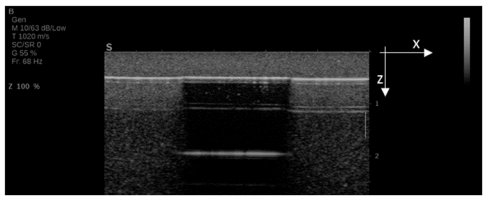

Fig. 6. Example of B-mode US image of a 6 cm^3 Sylgard inclusion in a Ecoflex phantom.

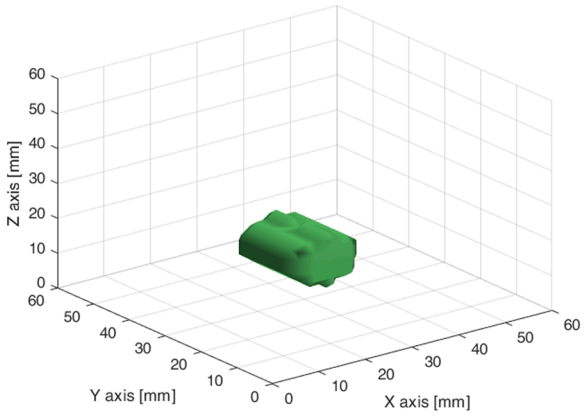

Fig. 7. 3D extrapolation from 2D segmentation of the big (6 cm^3) phantom inclusion.

- the inclusion reduced scattering coefficient ($\mu_{s,\ incl}^{'}$),
- the bulk absorption coefficient ($\mu_{a,\ bulk}$),
- the bulk reduced scattering coefficient ($\mu_{s,\ bulk}^{'}$),
- the inclusion size (1 or 6 cm^3).

As regards heterogeneous phantoms, the quality of the reconstruction of the inclusion volume and position (i.e., **localization** test) in the optical images is measured by considering the shift of the estimated coordinates and dimensions derived from the optical reconstruction performed with US prior with respect to the real ones.

Then, accuracy and linearity tests are employed on the analyzed data, obtained applying the heterogenous model described in Section 3.3 for Ecoflex phantoms and the homogenous one in Section 3.5 for resin phantoms.

The **accuracy** in the estimate of μ_a and $\mu_s^{'}$ is evaluated by comparing the measured values ($y_{measured}$) and the corresponding conventionally true values (y_{ctv}), as defined by Eq. (10):

$$Error = \frac{y_{measured} - y_{ctv}}{y_{ctv}} \times 100\ \% \tag{10}$$

The **linearity** assesses the system capability to linearly track changes in the measured optical properties of the inclusion and of the bulk. The R^2 squared coefficient [43] and the angular coefficient of the corresponding linear regression are used to estimate the quality of the results. In both cases, the ideal result is 1, implying a perfectly linear behavior along the diagonal.

The optical assessment of Ecoflex phantoms will be discussed considering different inclusion sizes and regularization parameters τ: 0.01 and 0.1. The values reported derive from the average over the pixels enclosed in the volumetric reconstruction of the inclusion or the complementary volume for the bulk. The availability of two acquisitions on the inclusion and two on the bulk gives rise to four possible inclusion-bulk couples. The plotted values are obtained by averaging over these four combinations. On the contrary, in the case of homogeneous resin phantoms, values derive from the average over all the available curves

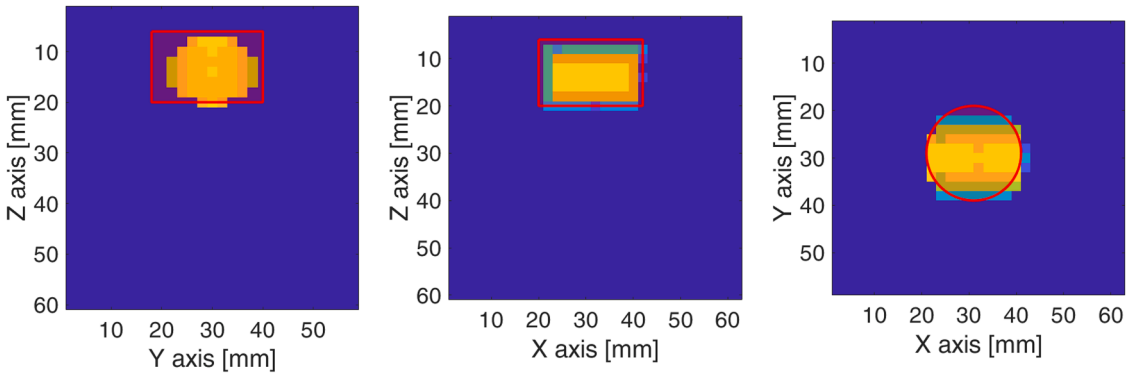

Fig. 8. Projections on the three orthogonal planes of the 3D inclusion reconstruction (big inclusion), summing overlapping pixels. The red profile marks the real position and shape. *xz* is the segmentation plane, while *yz* and *xy* the extrusion planes, where we expect less accuracy in localizing the inclusion.

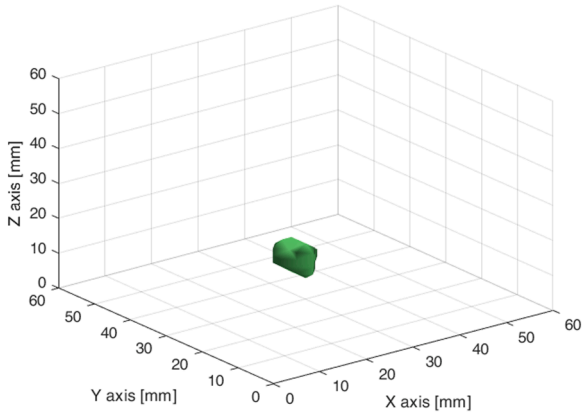

Fig. 9. 3D extrapolation from 2D segmentation of the small (1 cm^3) phantom inclusion.

of the four views, separately for each wavelength, and there is no use for the τ parameter.

5.3. Results

In the following, the results for the localization test and the outcomes for the accuracy and linearity tests are presented. Considerations about scattering always refer to the reduced scattering coefficient.

5.3.1. Inclusion localization

Fig. 6 reports the B-mode image (*xz* plane) of a SOLUS Ecoflex phantom, embedding a Sylgard inclusion covered by the 0.5 cm Ecoflex top layer. The inclusion is cylindrical, with the circular section parallel to the top *xy* plane.

The operator segments the inclusion on this bidimensional image, thus marking a rectangle profile. The resulting 3D extrapolation using the procedure described at Section 3.2 is depicted in Figs. 7 and 9 for the big and small inclusion, respectively. Figs. 8 and 10 illustrate the corresponding projections on the three orthogonal planes, summing overlapping pixels. The red profile marks the real position and shape of the inclusion. The central graph corresponds to the segmentation plane: indeed, it reproduces in both cases a rectangle, well contained in the expected borders. The other graphs show how the algorithm approximates the unknown dimensions rounding edges, which is correct for the

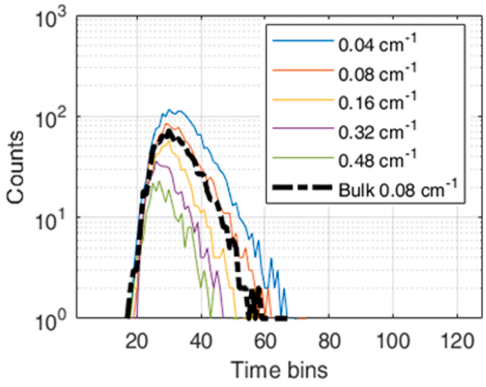

Fig. 11. DTOFs that intersect the big inclusion for different absorption coefficients. The inclusion depth is 0.5 cm from the top surface, the acquisition time 10 ms and the source-detector distance 2.83 cm.

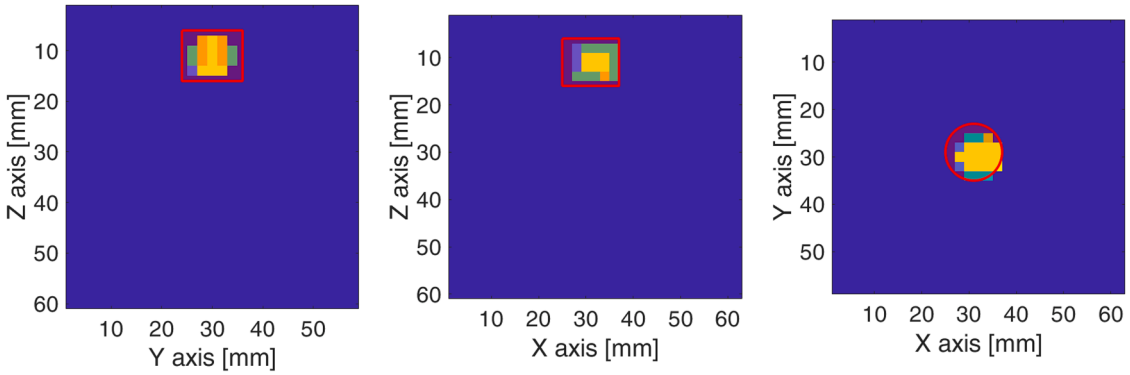

Fig. 10. Projections on the three orthogonal planes of the 3D inclusion reconstruction (small inclusion), summing overlapping pixels. The red profile marks the real position and shape. *xz* is the segmentation plane, while *yz* and *xy* the extrusion planes, where we expect less accuracy in localizing the inclusion.

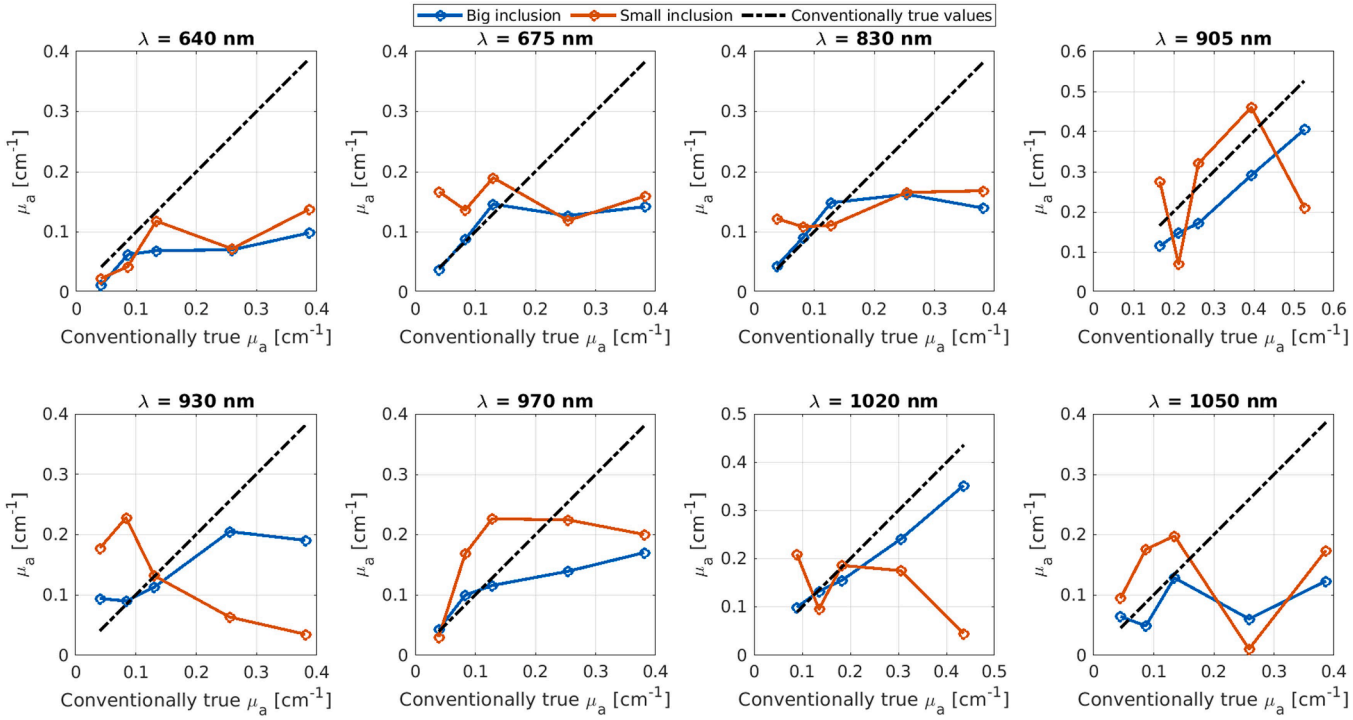

Fig. 12. Estimate of absorption coefficient of the inclusion in Ecoflex phantoms (obtained with $\tau = 0.01$).

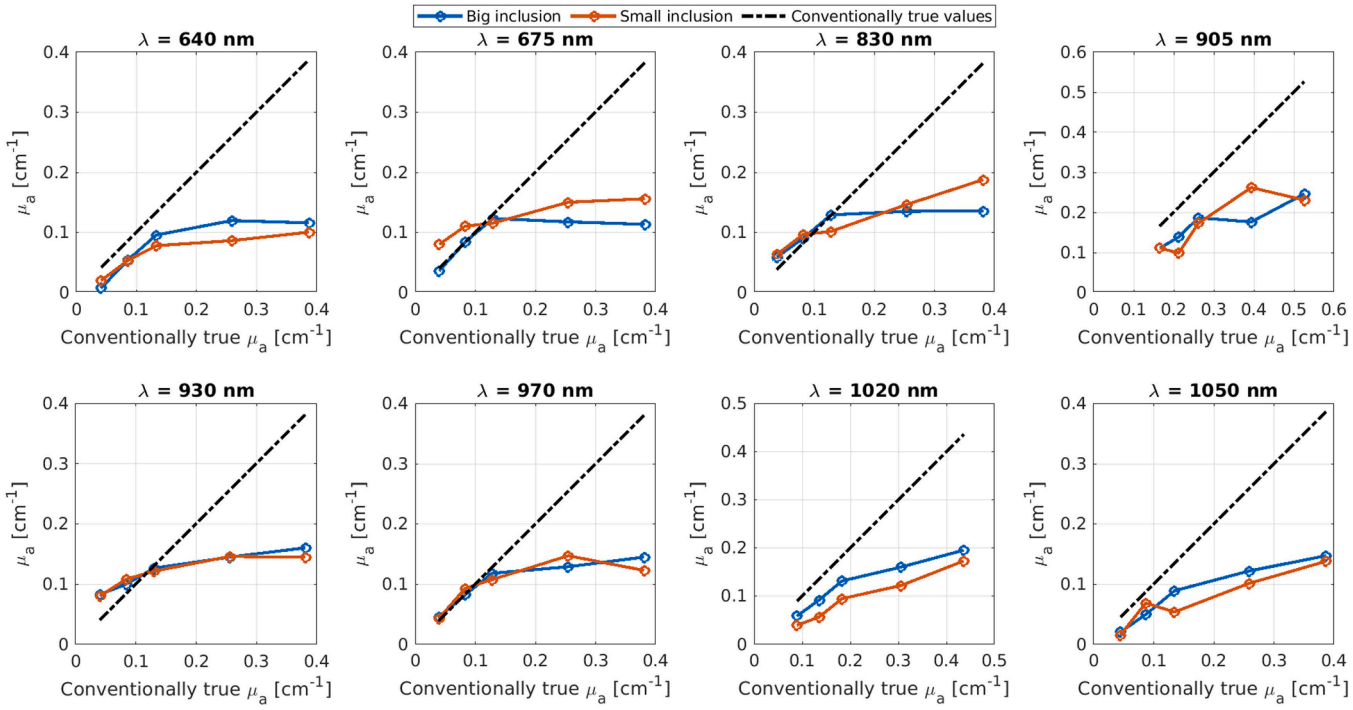

Fig. 13. Estimate of absorption coefficient of the inclusion in Ecoflex phantoms (obtained with $\tau = 0.1$).

xy plane (third plot), while it is less accurate for the *yz* plane (first plot).

The optimal localization of the inclusion is a clear consequence of the use of the US prior, with a maximum error of one pixel (2 mm) for the position and two pixels (4 mm) for the size along the extrusion direction.

5.3.2. Accuracy

In the following, the results of the accuracy test on heterogeneous phantoms are reported, combining three parameters:

- medium (five inclusions and three bulks),
- optical properties (absorption or scattering coefficient),
- regularization parameter ($\tau = 0.01$ and 0.1).

Data derive from the application of the analysis methods on the DTOFs generated during measurements. Fig. 11 depicts some examples of raw DTOFs at 640 nm associated to a source-detector distance equal to 2.83 cm, crossing the inclusion centre, with 10 ms as acquisition time.

Table 7
Relative errors on the inclusion absorption coefficient computed using Eq. (10), over wavelengths and inclusions. $\mu_a \leq 0.16$ cm^{-1} includes three inclusions and $\mu_a \leq 0.48$ cm^{-1} all the inclusions. Percentages are all positive because average and median values are computed using the absolute values of relative errors.

		Big inclusion		Small inclusion	
τ	Error	$\mu_a \leq 0.16$ cm^{-1}	$\mu_a \leq 0.48$ cm^{-1}	$\mu_a \leq 0.16$ cm^{-1}	$\mu_a \leq 0.48$ cm^{-1}
0.01	**Average**	26 %	35 %	88 %	76 %
	Median	15 %	27 %	57 %	57 %
0.1	**Average**	29 %	40 %	41 %	47 %
	Median	29 %	43 %	36 %	50 %

Colorful curves refer to different absorption coefficients for the inclusion, while the black dotted curve represents the bulk DTOF, as a reference (measurements from 1 to 5 in Table 6). Clear differences are observed on the trailing edge, as expected for different absorption values of the inclusion in TD: the higher the inclusion absorption, the lower the signal. Also, the lower the intensity, the higher the noise. Noise could be minimized by increasing the acquisition time. However, the time was tuned to ensure a complete DOT measurement in about one minute for the in vivo protocol.

5.3.2.1. Optical properties of the inclusion. In Figs. 12 and 13 (for $\tau =$ 0.01 and 0.1, respectively), each plot refers to a wavelength and the horizontal axis reports the conventionally true values. Hence, each point of the curves represents an inclusion. In each plot there are three curves: in orange the results for the small inclusion, in blue for the big inclusion, in black the conventionally true values.

In Fig. 12, at $\tau = 0.01$, we notice that, on the one hand, the values for the small and the big inclusions are quite different from each other (on average over inclusions and wavelengths, their percentage difference is 70 %, normalized to the big inclusion values). On the other hand, while reconstructions are good for $\mu_a \leq 0.16$ cm^{-1}, especially for the big inclusion (the median error is 15 %), the system strongly underestimates high absorption values (50 % as median relative error), as we can see from the last two points in each plot.

As the τ grows (Fig. 13), the results for the two inclusion sizes become more consistent (on average, their percentage difference is 24 % for $\tau = 0.1$, normalized to the big inclusion values), but, at the same time, underestimation is overall more and more marked, as shown in Table 7, considering the competition between smoothing effect and accuracy already mentioned in Section 3.4.

Let us now consider the estimate of the scattering properties of the inclusion (three values available). Observing Fig. 14, we can confirm that at the lower regularization value the orange and the blue curves are quite different (on average, the difference normalized to the big inclusion is 41 %). Also, the estimated values do not follow the increase in the nominal value and seem to be determined by to the bulk optical properties (nominally $\mu_s' = 12$ cm^{-1}, the same of the inclusion represented by the second point in each plot), irrespective of the change in μ_s' of the inclusion. A similar behavior is observed at a higher τ (Fig. 15), even though the smoothing effect determines a general improvement in accuracy, as confirmed in Table 8..

5.3.2.2. Bulk optical properties. We report only the results for the big inclusion at a single regularization parameter, because inclusion volume and regularization do not significantly affect the background estimation.

The accuracy for the absorption coefficient (Fig. 16, $\tau = 0.01$) is quite good in all cases: the ratio between nominal and measured values is on average 0.88 ± 0.22 over bulks and wavelengths, with a rather important underestimation (up to −49 %) at 640 and 905 nm.

Finally, as regards scattering, the system better tracks changes in the bulk μ_s' with respect to the inclusion one, even though the estimation of values higher than 15 cm^{-1} is not good, with errors up to −44 % at 640 nm (Fig. 17).

5.3.3. Linearity

5.3.3.1. Optical properties of the inclusion. Measuring linearity in terms of R^2 coefficient with reference to the previous figures, at the lowest regularization parameter the big inclusion returns more reliable values (on average over wavelengths $R^2 = 0.697 \pm 0.352$) with respect to the

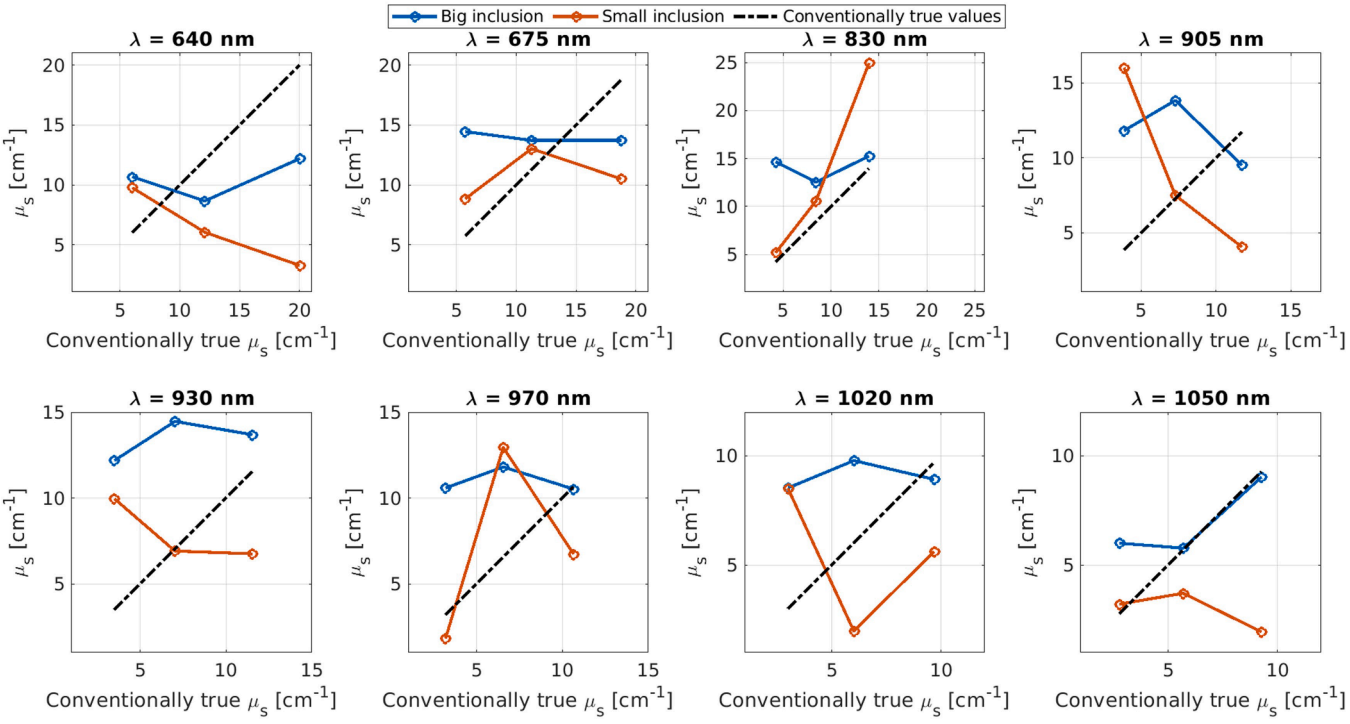

Fig. 14. Estimate of reduced scattering coefficient of the inclusion in Ecoflex phantoms (obtained with $\tau = 0.01$).

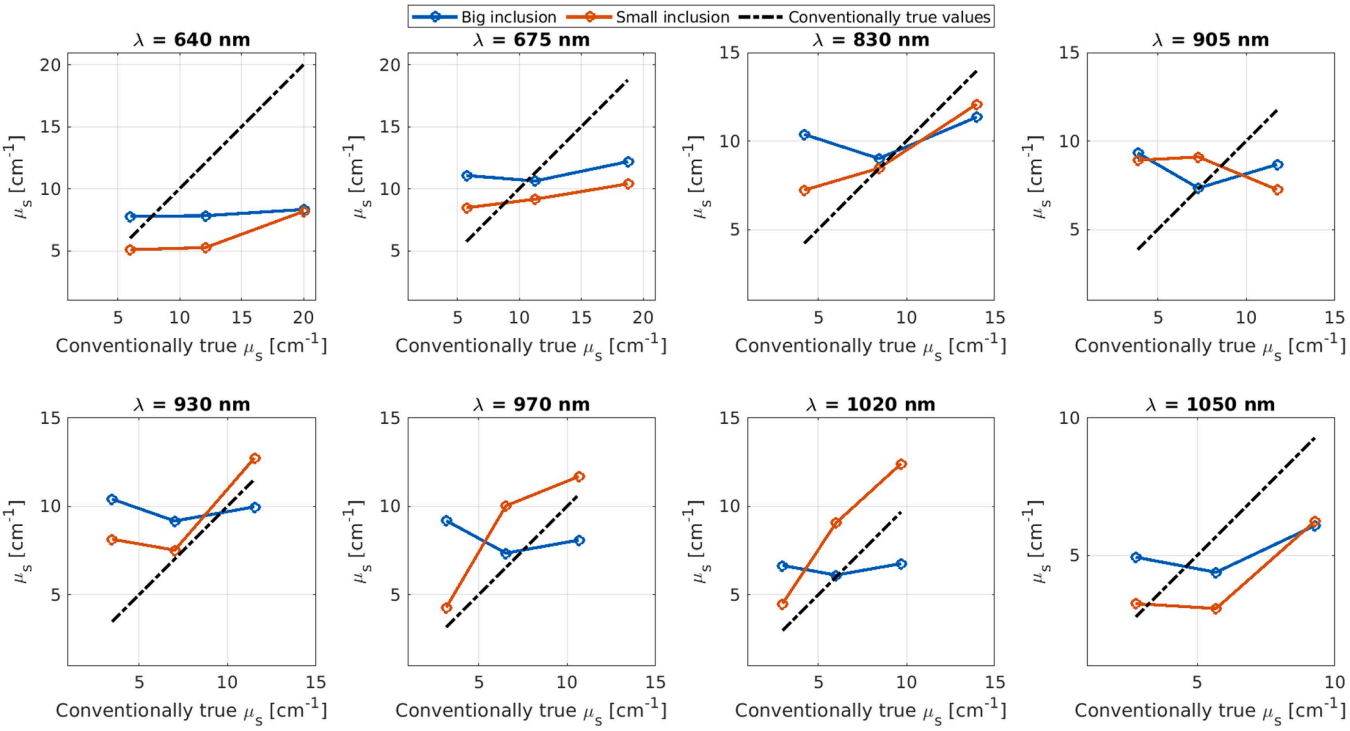

Fig. 15. Estimate of reduced scattering coefficient of the inclusion in Ecoflex phantoms (obtained with $\tau = 0.1$).

Table 8
Relative errors on the inclusion scattering coefficient computed using Eq. (10), over wavelengths and inclusions. Percentages are all positive because average and median values are computed using the absolute values of relative errors.

τ	Error	Big inclusion	Small inclusion
0.01	**Average**	85 %	69 %
	Median	56 %	47 %
0.1	**Average**	56 %	41 %
	Median	30 %	36 %

small one ($R^2 = 0.382 \pm 0.311$), as for the accuracy test ($\tau = 0.01$). Generally, the first three points of each curve (Fig. 12) are in agreement with expected values (for the big inclusion, on average $R^2 = 0.865 \pm 0.158$ and the angular coefficient is $m = 0.744 \pm 0.307$), while we denote a significant underestimation for absorption values higher than 0.16 cm^{-1}, causing a reduction in R^2, except for the wavelengths 905 and 1020 nm, which show a good linearity up to the most absorbing inclusion (0.48 cm^{-1}). This could depend on the available laser power (Table 2), that is on average higher at those two wavelengths.

As always, a higher τ makes the results for the big and the small inclusions more similar to each other, at the expenses of an even higher underestimation.

As already emerged from the accuracy test, results about scattering are not satisfying: in Figs. 14 and 15 no appreciable slope can be observed (average value over inclusions, wavelengths and τ equal to $m = 0.076 \pm 0.476$) and the trend is dominated by the background μ_s' regardless of the regularization.

5.3.3.2. Bulk optical properties. On the contrary, the results on the estimate of bulk optical properties are good for all the considered combinations. Linearity is optimal for the estimate of the absorption (R^2 ranging from 0.97 to 0.99), and good also for scattering (R^2 ranging from 0.77 to 0.98).

Finally, we tested absorption linearity over a broader range of absorption values (0.35 cm^{-1} instead of 0.16 cm^{-1}) using homogenous resin phantoms. This is useful to corroborate the quality of the bulk assessment already performed using Ecoflex phantoms over a more limited range of absorption properties.

Fig. 18 shows that, when considering the average over all the available source-detector distances, the probe measures absorption increments up to about 0.25 cm^{-1}. With homogeneous phantoms (using a homogeneous analysis model), R^2 ranges from 0.85 to 0.95, while the angular coefficient from 0.50 to 0.72, mostly affected by the highest absorbing phantom.

The bulk assessment through a homogenous model may be too rough an approximation in the case of an inclusion-embedding medium. However, this exercise can provide information of interest for spectroscopic applications other than breast cancer diagnosis, such as hemodynamics monitoring of brain activation and non-destructive characterizations of fruits quality.

6. Example of in vivo measurement

Finally, the outcome of a typical SOLUS in vivo measurement is presented to better illustrate the system operation. The measurement is carried out after the subject signed a written informed consent, under authorization of the Ethical Committee of IRCCS San Raffaele (Milan, Italy). The measurement followed the protocol described in Section 2.6.4 and aimed at retrieving the lesion and the surrounding healthy tissue composition. Based on our previous diffuse optical studies, a breast lesion usually manifests as an inhomogeneity due to fibrous tissue (i.e., high concentration of water, collagen and hemoglobin) in a more adipose background [44]. These properties are generally more marked in the case of malignant tumors rather than benign nodules, especially as regards collagen, which is a recognized risk factor for breast cancer, and blood, due to the angiogenesis notoriously linked to cancer progression. Also, malignant lesions are usually characterized by stiff tissue, as assessed by SWE [45] and irregular borders and they are taller-than-wide oriented [46].

As a case example, Fig. 19 depicts a 2.2 cm carcinoma using the techniques available on the SOLUS system.

Fig. 19A reports a B-mode image: the lesion borders are quite

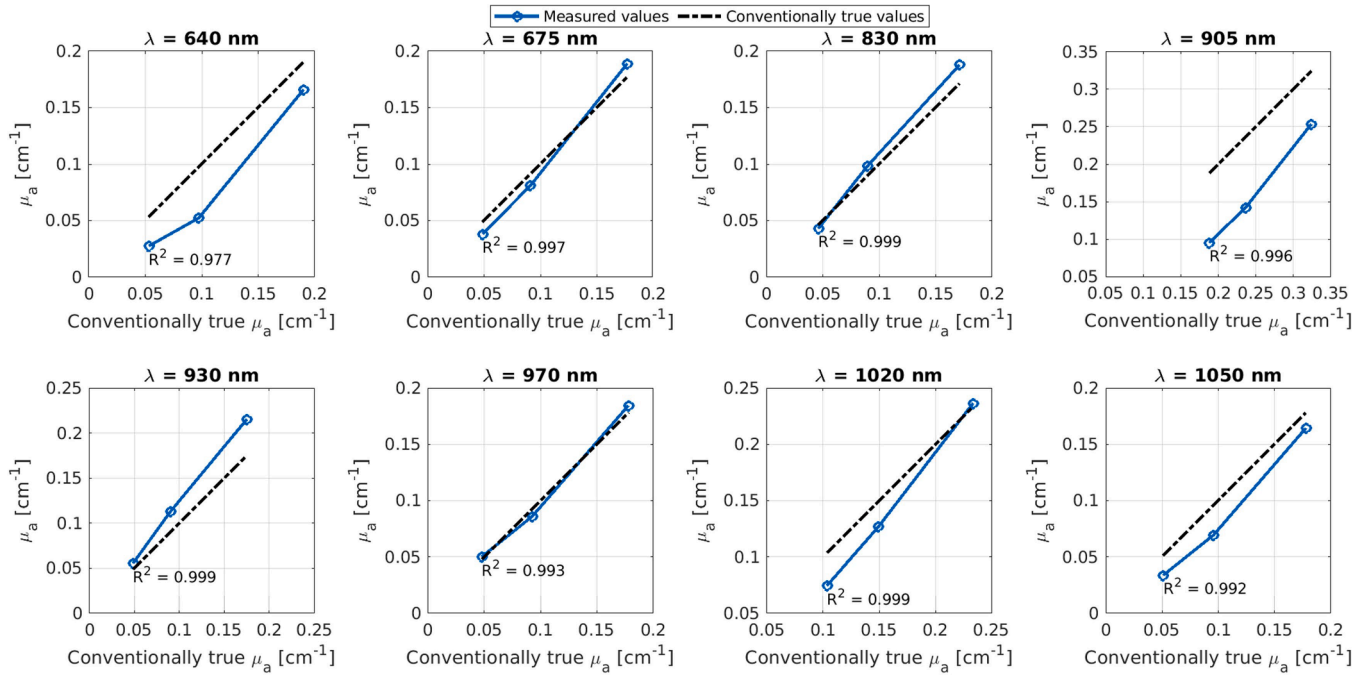

Fig. 16. Estimate of absorption coefficient of the bulk in Ecoflex phantoms (obtained with $\tau = 0.01$).

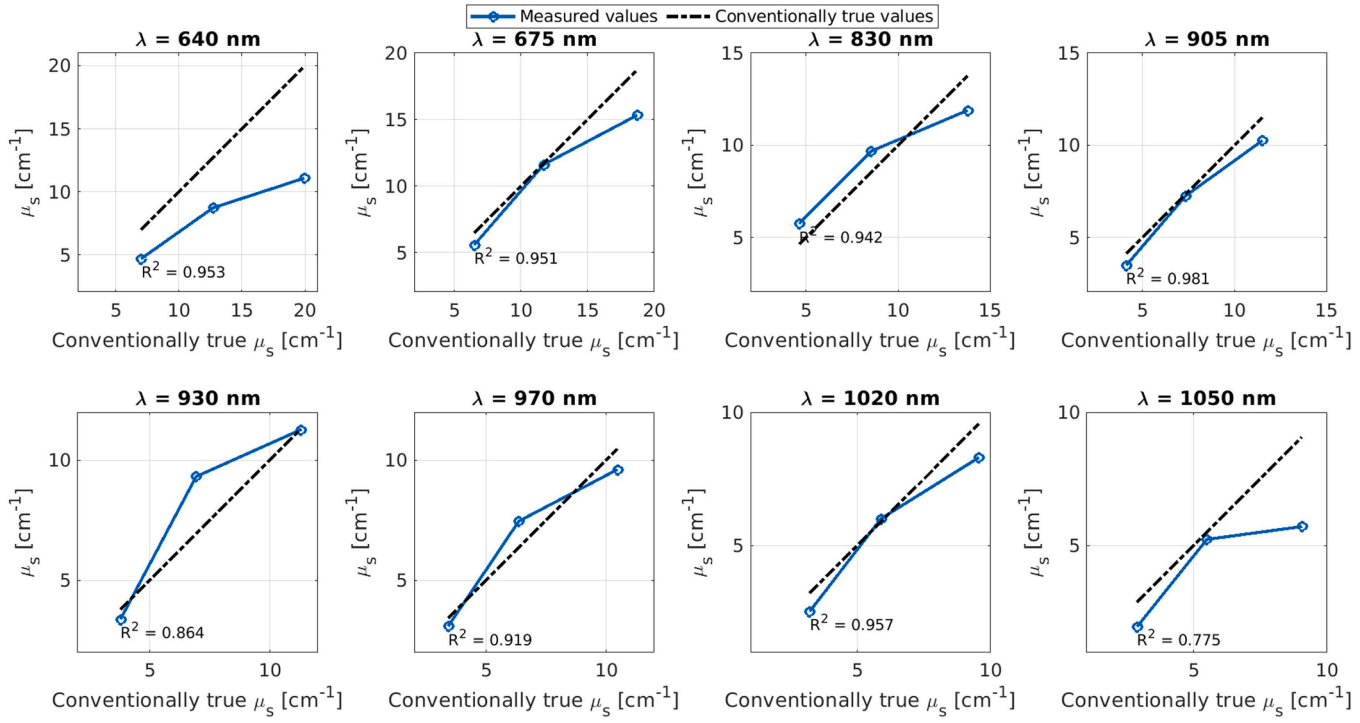

Fig. 17. Estimate of reduced scattering coefficient of the bulk in Ecoflex phantoms (obtained with $\tau = 0.01$).

irregular and it is taller-than-wide oriented. The operator segments the lesion (red contour) to provide a priori geometrical constraints to DOT, thus improving localization and quantification.

Panel B represents vascularization, obtained by CD, and shows a significant blood vessel that feeds the lesion.

SWE is illustrated in panel C, that demonstrates the very high stiffness of the lesion, quantitatively assessed as shown by the color bar on the right.

Figs. 20 and 21 represent an example of 3D optical reconstruction. In Fig. 20, panel A shows the volumetric morphological prior extracted from the bidimensional lesion segmentation. Panels B, C and D report one section along the *yz*, *xz* and *xy* planes respectively of the collagen map. First, we can observe that the lesion is well detected since DOT recognizes a contrast in composition between the lesion volume (demarcated by the black contour) and the outside healthy tissue. This is a clear consequence of the use of the morphological prior, as already described in Section 5.3. Yellow stands for high concentration, while blue means low concentration. Therefore, the lesion has a higher

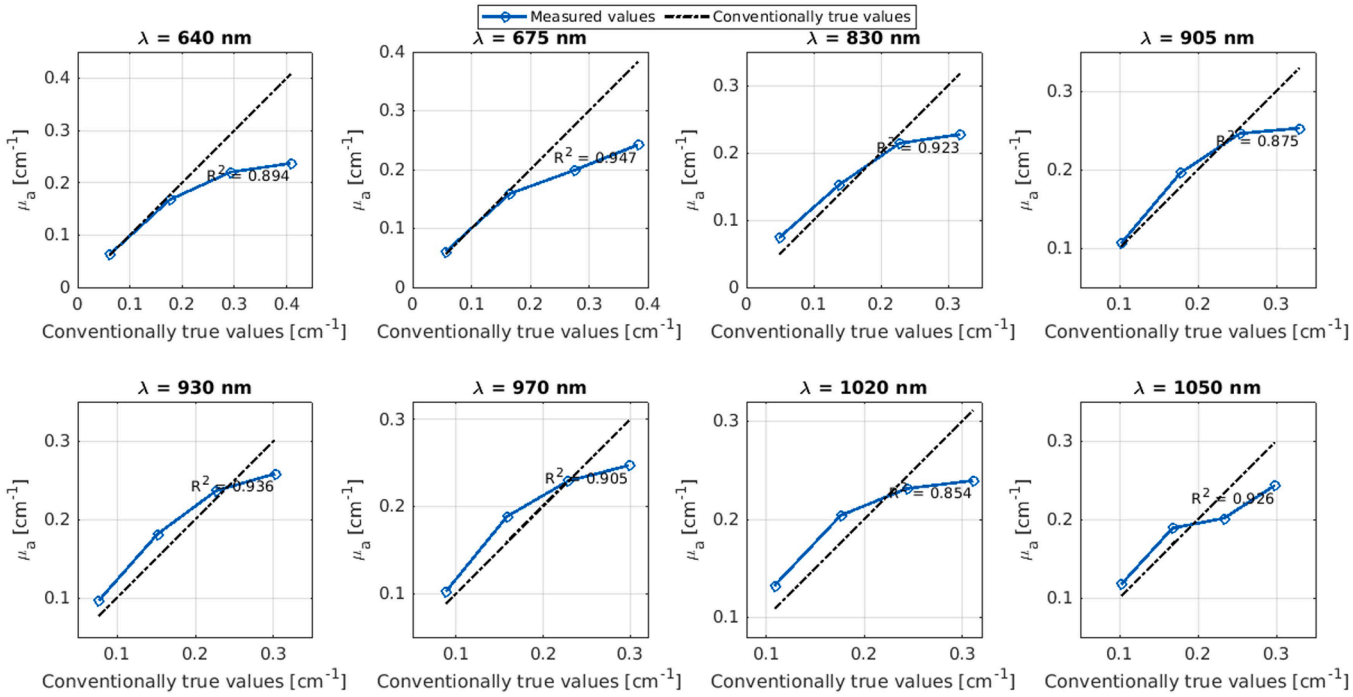

Fig. 18. Results for the linearity test on resin homogeneous phantoms averaging over all source-detector distances (absorption coefficients).

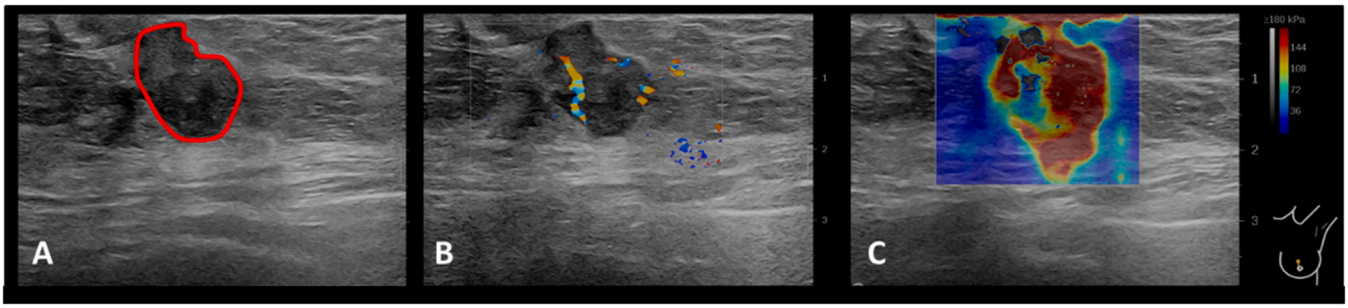

Fig. 19. B-mode (A) relative lesion segmentation, CD (B), SWE (C) images of a malignant lesion.

collagen concentration with respect to the surrounding healthy tissue, as expected. Also the other constituents contrasts are consistent with physiology parameters: the carcinoma is a fibrous agglomerate (i.e., higher water, collagen and hemoglobin content) in a lipidic background (Fig. 21). Contrasts directions are then correct and a systematic quantitative assessment will be proposed as soon as the clinical trial will be finished.

7. Discussion and conclusion

The optode represents the first ever miniaturization of time-resolved diffuse optics. This technological advancement was key to allow the implementation of a multimodal hand-held probe able to perform US-guided DOT for breast cancer diagnosis in TD.

Zhu's group has pioneered US-guided DOT applied to breast cancer applications, in frequency domain [47]. They investigated techniques for US-guided DOT reconstruction, deep-learning-based imaging [48], data optimization [49] and multimodal diagnosis [50].

This paper presents the strengths and the criticalities of the SOLUS system, to perform US-guided DOT in TD. Unlike continuous wave, both TD and frequency domain approaches offer the possibility to independently estimate absorption and scattering coefficients with a single source-detector pair [51,52]. However, time-resolved measurements are more informative since the delay of detected photons encodes the average depth investigated by such photons. Therefore, contributions coming from different depths in the medium can also be disentangled by considering different parts of the DTOF. For this reason, the TD approach is acknowledged as the one providing the largest information content. However, this occurs at the expense of a more complicated experimental setup. Also in light of this, the fabrication of the optode was a remarkable achievement.

We described in detail the technological implementation and performance of time-resolved US-guided DOT, and presented the characterization of the SOLUS hand-held probe focusing on optical data.

The study on heterogeneous and homogeneous tissue-mimicking phantoms helped assess the optical system performance: the lesion is efficiently located thanks to the use of the morphological prior. Besides, the reconstruction of the absorption coefficient of the bulk is good up to 0.25 cm^{-1} (relative error of 16 % on average over wavelengths and phantoms) and it reduces to 0.16 cm^{-1} for inclusions (on average, relative error of 26 %, $R^2 = 0.865 \pm 0.158$ and $m = 0.744 \pm 0.307$ for sufficiently big inhomogeneities and low regularization).

As regards scattering, the values for the bulk are measured quite consistently up to 15 cm^{-1} (relative error on average of 17 %), while the probe showed very low sensitivity to a localized perturbation. However, composition is a more crucial factor rather than microstructure for the

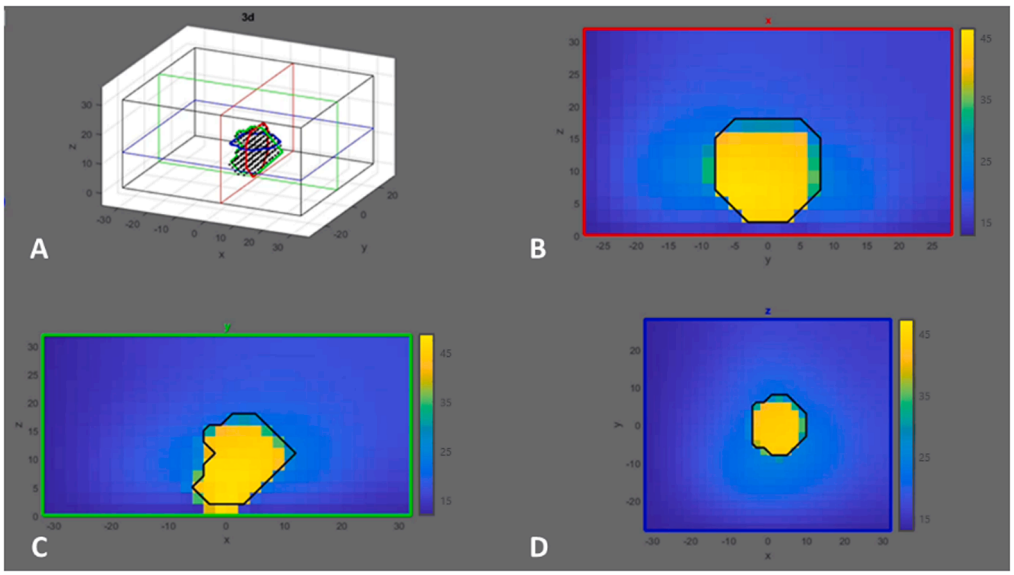

Fig. 20. Morphological prior extracted from lesion segmentation (A) used to guide DOT. Section (mm^2) of the 3D reconstructions of collagen concentration (mg/cm^3): *yz* plane (B), *xz* plane (C) and *xy* plane (D).

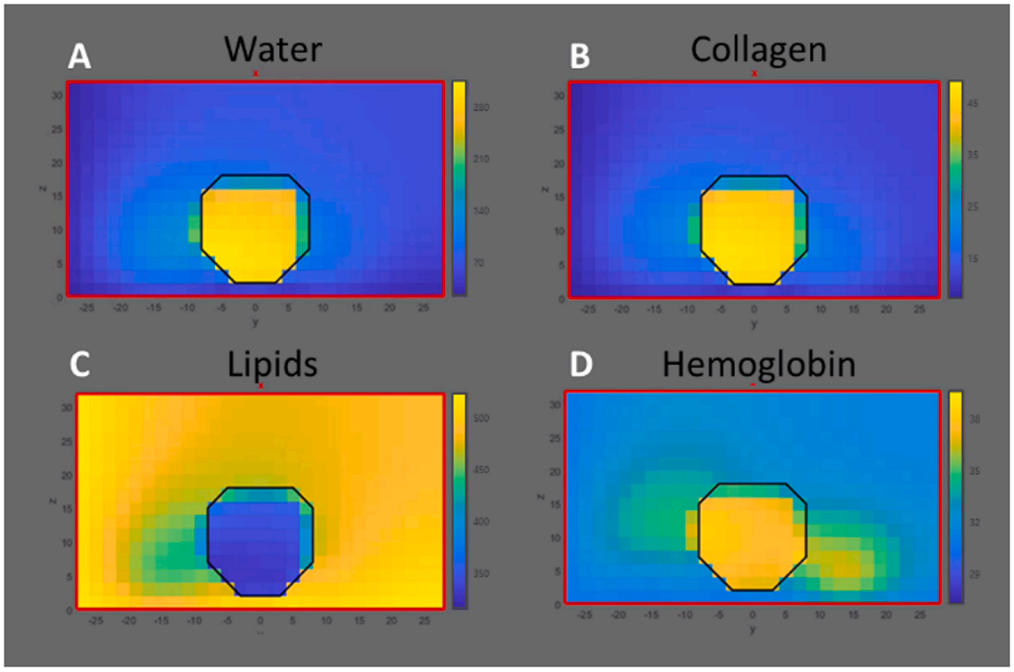

Fig. 21. *yz* (mm^2) section of water (A, mg/cm^3), collagen (B, mg/cm^3), lipids (C, mg/cm^3) and total hemoglobin (D, μM) concentrations.

discrimination of breast lesions. Then, a faint contrast in scattering between the lesion and the breast parenchyma may not be a significant hindrance.

In general, all errors go in the direction of underestimation, due to a combination of system performance, linear Born approximation, and effect of regularization.

To comprehensively test the coverage granted by these indicative limits (0.25 cm^{-1} for the bulk absorption and 15 cm^{-1} for the bulk scattering) across the absorption and scattering coefficient ranges of interest for the breast, we turn to an available historical dataset of in vivo measurements involving 218 patients [53]. This is useful to identify the most critical kinds of breast tissues and consequently estimate the extent of population that can be measured reliably with the SOLUS probe. This dataset was obtained using a time-resolved instrument developed by the research group at Politecnico di Milano to investigate breast tissue through diffuse optics. It includes bidimensional scans of the compressed breast in transmission mode in 4 projections (cranio-caudal right and left, oblique right and left) at 7 wavelengths: 635, 685, 785, 905, 930, 975, 1060 nm. Absorption coefficients were extracted via a homogenous approach to the diffusion equation for a slab geometry and then averaged over the scanned area (thus mixing healthy and possibly lesion tissue, but excluding marked inhomogeneities) and the projections for each patient.

Our purpose is to confront the SOLUS performance with a real scenario, i.e. to set the SOLUS efficiency limits with respect to a statistically significant in vivo dataset, hereby given by the historical study. The histograms in Figs. 22 and 23 report mean values vs. number of patients for absorption and scattering, respectively, drawing from the historical

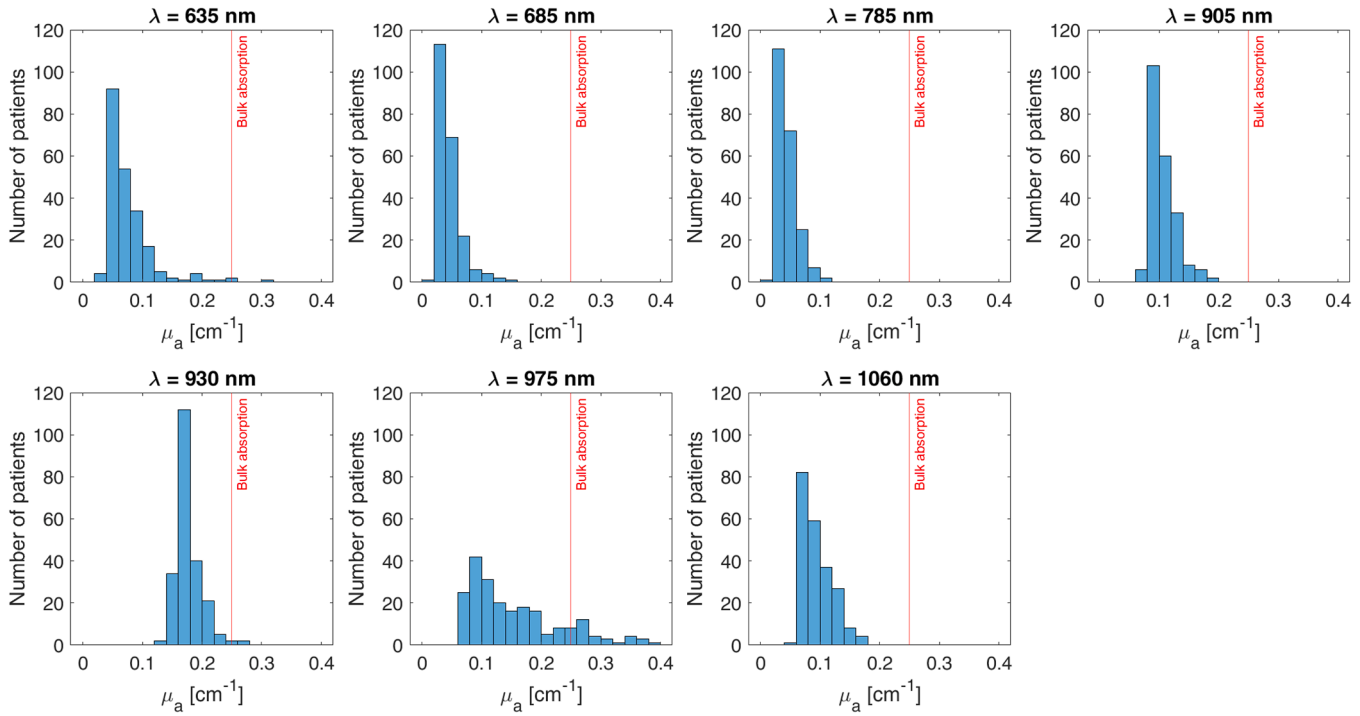

Fig. 22. Histograms representing mean absorption values vs. number of patients. Data derived from the historical dataset [53]. Red vertical line corresponds to the efficiency limit resulting from the SOLUS performance assessment.

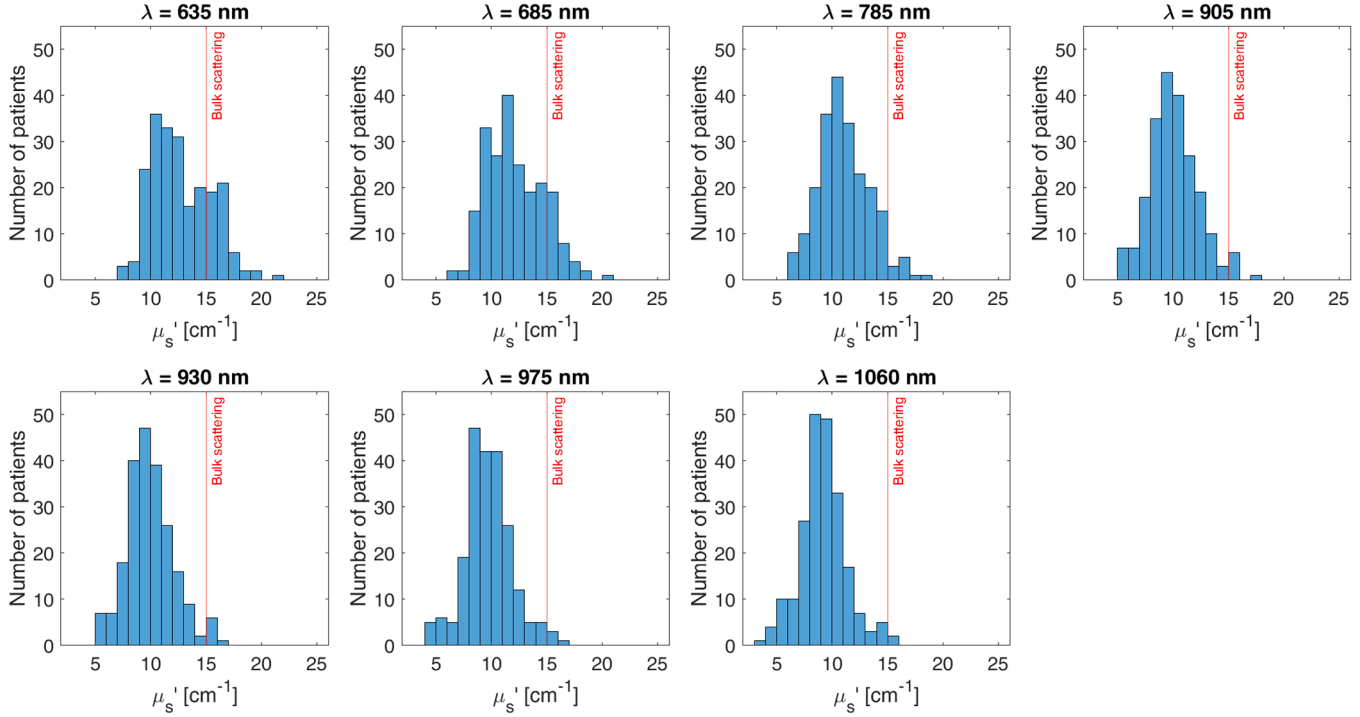

Fig. 23. Histograms representing mean reduced scattering values vs. number of patients. Data derived from the historical dataset [53]. Red vertical line corresponds to the efficiency limit resulting from the SOLUS performance assessment.

dataset. The red vertical lines correspond to the efficiency limits resulting from the SOLUS performance assessment. Table 9 estimates the percentages of population below this limit (i.e., those for which a SOLUS optical characterization of the bulk would be fair). Focusing on absorption, 975 nm (on the peak of water and close to 970 nm, available in SOLUS) appears as the most critical wavelength, while the others are satisfactorily within the SOLUS efficient range. This suggests that the estimate of water could be less reliable in the case of strongly dense (high water content) breasts. In particular, the 975 nm distribution appears as a right-skewed distribution with a broader extent, up to 0.4 cm^{-1}.

Hence, an extension of the efficiency range through more effective

Table 9
Indicative percentages of population for which the SOLUS probe would be reliable (i.e., fraction of patients participating in the historical clinical study, whose averaged optical values stay below the limits (reported in parenthesis) for an efficient optical characterization of the bulk through SOLUS). Data derived from [53].

λ [nm]	Bulk absorption (0.25 cm^{-1})	Bulk scattering (15 cm^{-1})
635	99 %	77 %
685	100 %	84 %
785	100 %	95 %
905	100 %	97 %
930	99 %	97 %
975	85 %	98 %
1060	100 %	99 %

data analysis methods could introduce a significant improvement in the bulk assessment. The same might occur for the lesion characterization.

Indeed, concerning the inclusion, the linear Born Approximation on one side grants an easy implementation and quick execution from a computational point of view, suitable for a real-time assessment in clinical settings (thus initially leading to this choice). On the other side, the linear approach intrinsically introduces a significant underestimation of the reconstructed optical properties in the case of big perturbations. Higher-order methods such as [54–56] could improve accuracy and consequently specificity and sensitivity in breast cancer diagnosis. Other than analytical methods, numerical and machine learning approaches could reach the same goal. These different approaches are under evaluation to identify the best choice allowing accurate results in real operation conditions.

The use of the historical dataset as a reference for the SOLUS instrument can provide useful information, but it should not be interpreted strictly, due the difficulty in comparing results among different photon migration instruments (as shown by the BITMAP exercise [57]), and to the mismatch of measurement conditions (reflectance vs. transmittance, homogeneous model vs. heterogeneous model, not identical wavelengths). Furthermore, the historical dataset consists of average values that mix healthy and possibly unhealthy tissue, thus preventing the computation of background vs. lesion ratios, which would be of utmost interest for the perturbation problem object of SOLUS analysis. However, marked inhomogeneities within a breast were excluded from calculations made to estimate the average properties of that breast. Thus, the distributions shown in Figs. 22 and 23 are expected to be close to the average properties of healthy tissue.

This estimate suggests that the SOLUS approach could be effective for a large part of breast tissues. A full performance assessment for lesion characterization is extremely complex, depending on the optical properties of both lesion and healthy tissue, but also on lesion size and depth. We will be able to confirm our estimate on the capability to characterize healthy tissue and we will investigate lesion characterization when real patient data become available at the end of the SOLUS clinical trial.

Regarding the quantification of tissue composition, to our knowledge, no phantoms are available to mimic tissue composition in terms of all 5 constituents considered in our study, that are water, lipid, collagen and blood parameters, and no other technique is available to measure bulk (deep) tissue composition non-invasively for a comparative in vivo assessment. With in vivo measurements, we can check whether our estimates correlate with tissue physiology or pathology. That does not provide a quantification of the accuracy, but rather tells us how effective we are at our diagnostic aim. The clinical validation will tell us how effective the instrument is to discriminate lesions.

In conclusion, we presented the performance assessment of the prototype of a multimodal hand-held probe for tomographic imaging, whose break-through element is the “optode”, a stand-alone module for time-resolved spectroscopy.

The results reported here are the starting point for the research of more efficient strategies for data analysis. For example, as an initial step, we have only considered data collected in the first detector hardware gate, similar to a free running acquisition. The use of gated curves is expected to enhance sensitivity to absorption and deep layers. Tests on phantoms are planned to verify the efficiency of the gating algorithm and the improvement in accuracy and linearity. Also, non-linear models or artificial intelligence approaches could highlight contrasts, not only as alternative means to retrieve the optical properties, but also as a posteriori correction based on the phantom assessment results. Furthermore, outcomes could benefit from the application of a spectral fit, intended to retrieve directly the constituents’ concentrations rather than the optical properties. In fact, the reduction of the number of fitting variables has already proved effective in providing more robust results, especially when a limited number of wavelengths is available.

Future work will help define a more robust optical assessment to highlight the informative content of the SOLUS dataset for a thorough multimodal evaluation of breast lesions. In parallel, the clinical validation of the instrument is providing real data that will help optimize the analysis approaches and procedures.

Finally, although this study was centered on breast cancer imaging utilizing an 8-optode probe, it is important to note that the individual optode opens up exciting possibilities for wearable applications of diffuse optics, including monitoring of hemodynamics and tracking of brain activation, as previously explored [58], as well as non-destructive quality assessment for industrial-level fruit inspection. These diverse fields represent promising avenues for future exploration.

CRediT authorship contribution statement

Giulia Maffeis: Validation, Investigation, Data curation, Writing – original draft. **Laura Di Sieno:** Conceptualization, Validation, Data curation, Writing – review & editing. **Alberto Dalla Mora:** Conceptualization, Validation, Data curation, Writing – review & editing. **Antonio Pifferi:** Conceptualization, Investigation, Formal analysis, Supervision, Data curation. **Alberto Tosi:** Methodology, Validation, Resources. **Enrico Conca:** Validation, Resources. **Andrea Giudice:** Methodology, Validation, Resources. **Alessandro Ruggeri:** Validation, Resources, Software, Writing – review & editing. **Simone Tisa:** Validation, Resources, Software, Writing – review & editing. **Alexander Flocke:** Validation, Resources. **Bogdan Rosinski:** Validation, Resources, Writing – review & editing. **Jean-Marc Dinten:** Methodology, Validation, Supervision. **Mathieu Perriollat:** Validation, Investigation, Software. **Jonathan Lavaud:** Validation, Resources, Writing – review & editing. **Simon Arridge:** Conceptualization, Formal analysis, Supervision, Software. **Giuseppe Di Sciacca:** Validation, Investigation, Software, Data curation. **Andrea Farina:** Validation, Software. **Pietro Panizza:** Validation, Resources. **Elena Venturini:** Validation, Resources. **Peter Gordebeke:** Visualization. **Paola Taroni:** Project administration, Funding acquisition, Conceptualization, Methodology, Supervision, Formal analysis, Writing – review & editing.

Declaration of competing interest

The authors declare that they have no known competing financial interests or personal relationships that could have appeared to influence the work reported in this paper.

Data availability

The datasets generated during and analysed during the current study are available from the corresponding author on reasonable request.

Acknowledgment

This project has received fundings from the European Union’s Horizon 2020 Research and Innovation Programme under grant agreement

no. 731877. The project is an initiative of the Photonics Public Private Partnership.

References

[1] Sung H, Ferlay J, Siegel RL, Laversanne M, Soerjomataram I, Jemal A, Bray F. Global cancer statistics 2020: GLOBOCAN estimates of incidence and mortality worldwide for 36 cancers in 185 countries. CA Cancer J Clin 2021;71(3):209–49.

[2] Sree SV. Breast imaging: a survey. World J Clin Oncol 2011;2(4):171.

[3] Iranmakani S, Mortezazadeh T, Sajadian F, Ghaziani MF, Ghafari A, Khezerloo D, Musa AE. A review of various modalities in breast imaging: technical aspects and clinical outcomes. Egypt J Radiol Nucl Med 2020;51(1):57.

[4] Ho T-QH, Bissell MCS, Kerlikowske K, Hubbard RA, Sprague BL, Lee CI, Tice JA, Tosteson ANA, Miglioretti DL. Cumulative probability of false-positive results after 10 years of screening with digital breast tomosynthesis vs. digital mammography. JAMA Netw Open 2022;5(3):e222440.

[5] Elmore JG, Barton MB, Moceri VM, Polk S, Arena PJ, Fletcher SW. Ten-year risk of false positive screening mammograms and clinical breast examinations. N Engl J Med 1998;338(16):1089–96.

[6] DeFrank JT, Rimer BK, Bowling JM, Earp JA, Breslau ES, Brewer NT. Influence of false-positive mammography results on subsequent screening: do physician recommendations buffer negative effects? J Med Screen 2012;19(1):35–41.

[7] Tromberg BJ, Pogue BW, Paulsen KD, Yodh AG, Boas DA, Cerussi AE. Assessing the future of diffuse optical imaging technologies for breast cancer management. Med Phys 2008;35(6Part1):2443–51.

[8] Grosenick D, Rinneberg H, Cubeddu R, Taroni P. Review of optical breast imaging and spectroscopy. J Biomed Opt 2016;21(9):091311.

[9] Leff DR, Warren OJ, Enfield LC, Gibson A, Athanasiou T, Patten DK, Hebden J, Yang GZ, Darzi A. Diffuse optical imaging of the healthy and diseased breast: a systematic review. Breast Cancer Res Treat 2008;108(1):9–22.

[10] Gibson A, Dehghani H. Diffuse optical imaging. Philos Trans R Soc A Math Phys Eng Sci 2009;367(1900):3055–72.

[11] Taroni P. Diffuse optical imaging and spectroscopy of the breast: a brief outline of history and perspectives. Photochem Photobiol Sci 2012;11(2):241–50.

[12] Taroni P, Dalla Mora A, Di Sieno L, Maffeis G, Pifferi A, Tosi A, Conca E, Giudice A, Ruggeri A, Tisa S, Flocke A, Rosinski B, Dinten J-M, Perriollat M, Blanquer G, Fraschini C, Lavaud J, Arridge S, Di Sciacca G, Farina A, Gordebeke P, Venturini E, Panizza P. SOLUS: multimodal system combining ultrasounds and diffuse optics for tomographic imaging of breast cancer. In: Biophotonics congress: biomedical optics 2022 (Translational, Microscopy, OCT, OTS, Brain). Optica Publishing Group; 2022. TTu2B.1.

[13] Pifferi A, Dalla Mora A, Di Sieno L, Ferocino E, Tosi A, Conca E, Sesta V, Giudice A, Ruggeri A, Tisa S, Flocke A, Rosinski B, Dinten J-M, Perriollat M, Fraschini C, Sportouche H, Arridge S, Di Sciacca G, Farina A, Panizza P, Venturini E, Gordebeke P, Zolda P, Taroni P. SOLUS: an innovative multimodal imaging system to improve breast cancer diagnosis through diffuse optics and ultrasounds. In: Fantini S, Taroni P, editors. Optical tomography and spectroscopy of tissue XIV. SPIE; 2021. p. 8. 2021.

[14] Di Sieno L, Dalla Mora A, Ferocino E, Pifferi A, Tosi A, Conca E, Sesta V, Giudice A, Ruggeri A, Tisa S, Flocke A, Rosinski B, Dinten JM, Perriollat M, Savery D, Sportouche H, Arridge S, Farina A, Panizza P, Venturini E, Gordebeke P, Zolda P, Taroni P. SOLUS project: bringing innovation into breast cancer diagnosis and in the time-domain diffuse optical field. In: Opt. InfoBase conf. pap. Part F179; 2020. p. 2–3.

[15] Di Sieno L, Maffeis G, Dalla Mora A, Ferocino E, Tosi A, Conca E, et al. Smart optode for 8-wavelength time-gated diffuse optics. IEEE J Sel Top Quantum Electron 2023:1–10. https://doi.org/10.1109/JSTQE.2023.3321436.

[16] Di Sciacca G, Maffeis G, Farina A, Dalla Mora A, Pifferi A, Taroni P, Arridge S. Evaluation of a pipeline for simulation, reconstruction, and classification in ultrasound-aided diffuse optical tomography of breast tumors. J Biomed Opt 2022;27(03):1–19.

[17] Di Sciacca G, Di Sieno L, Farina A, Lanka P, Venturini E, Panizza P, Dalla Mora A, Pifferi A, Taroni P, Arridge SR. Enhanced diffuse optical tomographic reconstruction using concurrent ultrasound information. Philos Trans R Soc A Math Phys Eng Sci 2021;379(2204):20200195.

[18] Vavadi H, Mostafa A, Zhou F, Uddin KMS, Althobaiti M, Xu C, Bansal R, Ademuyiwa F, Poplack S, Zhu Q. Compact ultrasound-guided diffuse optical tomography system for breast cancer imaging. J Biomed Opt 2018;24(02):1.

[19] Zhi W, Wang Y, Chang C, Wang F, Chen Y, Hu N, Zhu X, Xie L. US-guided diffuse optical tomography: clinicopathological features affect total hemoglobin concentration in breast cancer. Transl Oncol 2018;11(4):845–51.

[20] Wu T, Feng J-C, Tuerhong S, Wang B, Yang L, Zhao Q, Dilixiati J, Xu W-T, Zhu L-P. Ultrasound-guided diffuse optical tomography for differentiation of benign and malignant breast lesions: a meta-analysis. J Ultrasound Med 2017;36(3):485–92.

[21] Althobaiti M, Vavadi H, Zhu Q. Diffuse optical tomography reconstruction method using ultrasound images as prior for regularization matrix. J Biomed Opt 2017;22(2):026002.

[22] Yuan Z, Zhang Q, Sobel ES, Jiang H. High-resolution x-ray guided three-dimensional diffuse optical tomography of joint tissues in hand osteoarthritis: morphological and functional assessments. Med Phys 2010;37(8):4343–54.

[23] Yun S, Kim Y, Kim H, Lee S, Jeong U, Lee H, Choi Y, Cho S. Three-compartment-breast (3CB) prior-guided diffuse optical tomography based on dual-energy digital breast tomosynthesis (DBT). Biomed Opt Express 2021;12(8):4837.

[24] Feng J, Zhang W, Li Z, Jia K, Jiang S, Dehghani H, Pogue BW, Paulsen KD. Deep-learning based image reconstruction for MRI-guided near-infrared spectral tomography. Optica 2022;9(3):264.

[25] Muldoon A, Kabeer A, Cormier J, Saksena MA, Fang Q, Carp SA, Deng B. Method to improve the localization accuracy and contrast recovery of lesions in separately acquired X-ray and diffuse optical tomographic breast imaging. Biomed Opt Express 2022;13(10):5295.

[26] Zimmermann BB, Deng B, Singh B, Martino M, Selb J, Fang Q, Sajjadi AY, Cormier J, Moore RH, Kopans DB, Boas DA, Saksena MA, Carp SA. Multimodal breast cancer imaging using coregistered dynamic diffuse optical tomography and digital breast tomosynthesis. J Biomed Opt 2017;22(4):046008.

[27] Brooksby B, Pogue BW, Jiang S, Dehghani H, Srinivasan S, Kogel C, Tosteson TD, Weaver J, Poplack SP, Paulsen KD. Imaging breast adipose and fibroglandular tissue molecular signatures by using hybrid MRI-guided near-infrared spectral tomography. Proc Natl Acad Sci 2006;103(23):8828–33.

[28] H.S. Imagine, "AIXPLORER MACH 30," Available at: https://www.hologic.com/sites/default/files/2021-07/Mach-30_Brochure.pdf. Accessed: 18/Feb./2023.

[29] H.S. Imagine, "SuperSonic Mach 30, Ultrasound imaging platform," Available at: https://www.hologic.com/sites/default/files/2020_11/PM-EC-094-RevA-SuperSonic-MACH-30-sw-V2-System-Specifications-USA.pdf. Accessed: 18/Feb./2023.

[30] Di Sieno L, Ferocino E, Conca E, Sesta V, Buttafava M, Villa F, Zappa F, Contini D, Torricelli A, Taroni P, Tosi A, Pifferi A, Mora AD. Time-domain diffuse optics with 8.6 mm 2 fast-gated SiPM for extreme light harvesting. Opt Lett 2021;46(2):424.

[31] Conca E, Sesta V, Buttafava M, Villa F, Di Sieno L, Dalla Mora A, Contini D, Taroni P, Torricelli A, Pifferi A, Zappa F, Tosi A. Large-area, fast-gated digital SiPM with integrated TDC for portable and wearable time-domain NIRS. IEEE J Solid-State Circuits 2020;55(11):3097–111.

[32] Dalla Mora A, Tosi A, Zappa F, Cova S, Contini D, Pifferi A, Spinelli L, Torricelli A, Cubeddu R. Fast-gated single-photon avalanche diode for wide dynamic range near infrared spectroscopy. IEEE J Sel Top Quantum Electron 2010;16(4):1023–30.

[33] Pirovano I, Re R, Candeo A, Contini D, Torricelli A, Spinelli L. Instrument response function acquisition in reflectance geometry for time-resolved diffuse optical measurements. Biomed Opt Express 2020;11(1):240.

[34] Di Sieno L, Contini D, Presti GLo, Cortese L, Mateo T, Rosinski B, Venturini E, Panizza P, Mora M, Aranda G, Squarcia M, Farina A, Durduran T, Taroni P, Pifferi A, Mora AD. Systematic study of the effect of ultrasound gel on the performances of time-domain diffuse optics and diffuse correlation spectroscopy. Biomed Opt Express 2019;10(8):3899.

[35] Kass M, Witkin A, Terzopoulos D. Snakes: active contour models. Int J Comput Vis 1988;1(4):321–31.

[36] Guven M, Yazici B, Kwon K, Giladi E, Intes X. Effect of discretization error and adaptive mesh generation in diffuse optical absorption imaging: I. Inverse Probl 2007;23(3):1115–33.

[37] D'Andrea C, Spinelli L, Bassi A, Giusto A, Contini D, Swartling J, Torricelli A, Cubeddu R. Time-resolved spectrally constrained method for the quantification of chromophore concentrations and scattering parameters in diffusing media. Opt Express 2006;14(5):1888.

[38] Martelli F, Del Bianco S, Ismaelli A, Zaccanti G. Light propagation through biological tissue and other diffusive media: theory, solutions, and software. SPIE; 2009.

[39] C.I. Electrotechnical, "Medical electrical equipment—Part 2–37: particular requirements for the basic safety and essential performance of ultrasonic medical diagnostic and monitoring equipment," Available at: https://webstore.iec.ch/publication/22634. Accessed: 12/Jul./2023.

[40] Di Sieno L, Cubeddu R, Sportouche H, Savéry D, Konugolu Venkata Sekar S, Rosinski B, Farina A, Ferocino E, Lanka P, Taroni P, Pifferi A, Dalla Mora A. Solid heterogeneous phantoms for multimodal ultrasound and diffuse optical imaging: an outcome of the SOLUS project for standardization. In: Amelink A, Nadkarni SK, editors. Novel biophotonics techniques and applicationsv. SPIE; 2019. p. 39. Part F142-(November 2016).

[41] Konugolu Venkata Sekar S, Dalla Mora A, Bargigia I, Martinenghi E, Lindner C, Farzam P, Pagliazzi M, Durduran T, Taroni P, Pifferi A, Farina A. Broadband (600–1350 nm) time-resolved diffuse optical spectrometer for clinical use. IEEE J Sel Top Quantum Electron 2016;22(3):406–14.

[42] Pifferi A, Torricelli A, Bassi A, Taroni P, Cubeddu R, Wabnitz H, Grosenick D, Möller M, Macdonald R, Swartling J, Svensson T, Andersson-Engels S, van Veen RLP, Sterenborg HJCM, Tualle J-M, Nghiem HL, Avrillier S, Whelan M, Stamm H. Performance assessment of photon migration instruments: the MEDPHOT protocol. Appl Opt 2005;44(11):2104.

[43] Chicco D, Warrens MJ, Jurman G. The coefficient of determination R-squared is more informative than SMAPE, MAE, MAPE, MSE and RMSE in regression analysis evaluation. PeerJ Comput Sci 2021;7:e623.

[44] Quarto G, Spinelli L, Pifferi A, Torricelli A, Cubeddu R, Abbate F, Balestreri N, Menna S, Cassano E, Taroni P. Estimate of tissue composition in malignant and benign breast lesions by time-domain optical mammography. Biomed Opt Express 2014;5(10):3684.

[45] Liu B, Zheng Y, Huang G, Lin M, Shan Q, Lu Y, Tian W, Xie X. Breast lesions: quantitative diagnosis using ultrasound shear wave elastography—A systematic review and meta-analysis. Ultrasound Med Biol 2016;42(4):835–47.

[46] A. C. of Radiology, "BI-RADS Reporting Systems," Available at: https://www.acr.org/-/media/ACR/Files/RADS/BI-RADS/Mammography-Reporting.pdf. Accessed: 06/Dec./2022.

[47] Zhu Q, Cronin EB, Currier AA, Vine HS, Huang M, Chen N, Xu C. Benign versus malignant breast masses: optical differentiation with US-guided optical imaging reconstruction. Radiology 2005;237(1):57–66.

[48] Zou Y, Zeng Y, Li S, Zhu Q. Machine learning model with physical constraints for diffuse optical tomography. Biomed Opt Express 2021;12(9):5720.
[49] Xu S, Shihab Uddin KM, Zhu Q. Improving DOT reconstruction with a Born iterative method and US-guided sparse regularization. Biomed Opt Express 2019; 10(5):2528.
[50] Uddin KMS, Zhang M, Anastasio M, Zhu Q. Optimal breast cancer diagnostic strategy using combined ultrasound and diffuse optical tomography. Biomed Opt Express 2020;11(5):2722.
[51] Yamada Y, Suzuki H, Yamashita Y. Time-domain near-infrared spectroscopy and imaging: a review. Appl Sci 2019;9(6):1127.
[52] Pifferi A, Contini D, Dalla Mora A, Farina A, Spinelli L, Torricelli A. New frontiers in time-domain diffuse optics, a review. J Biomed Opt 2016;21(9):091310.
[53] Taroni P, Paganoni AM, Ieva F, Pifferi A, Quarto G, Abbate F, Cassano E, Cubeddu R. Non-invasive optical estimate of tissue composition to differentiate malignant from benign breast lesions: a pilot study. Sci Rep 2017;7(1):40683.
[54] Grosenick D, Kummrow A, Macdonald R, Schlag PM, Rinneberg HH. Evaluation of higher-order time-domain perturbation theory of photon diffusion on breast-equivalent phantoms and optical mammograms. Phys Rev E 2007;76(6):061908.
[55] Wassermann B, Jishi RA, Grosenick D. Efficient algorithm to calculate the optical properties of breast tumors by high-order perturbation theory. J Opt Soc Am A 2023;40(10):1882.
[56] Sassaroli A, Martelli F, Fantini S. Perturbation theory for the diffusion equation by use of the moments of the generalized temporal point-spread function III Frequency-domain and time-domain results. J Opt Soc Am A 2010;27(7):1723.
[57] Lanka P, Yang L, Orive-Miguel D, Veesa JD, Tagliabue S, Sudakou A, Samaei S, Forcione M, Kovacsova Z, Behera A, Gladytz T, Grosenick D, Hervé L, Durduran T, Bejm K, Morawiec M, Kacprzak M, Sawosz P, Gerega A, Liebert A, Belli A, Tachtsidis I, Lange F, Bale G, Baratelli L, Gioux S, Alexander K, Wolf M, Sekar SKV, Zanoletti M, Pirovano I, Lacerenza M, Qiu L, Ferocino E, Maffeis G, Amendola C, Colombo L, Frabasile L, Levoni P, Buttafava M, Renna M, Di Sieno L, Re R, Farina A, Spinelli L, Dalla Mora A, Contini D, Taroni P, Tosi A, Torricelli A, Dehghani H, Wabnitz H, Pifferi A. Multi-laboratory performance assessment of diffuse optics instruments: the BitMap exercise. J Biomed Opt 2022;27(07):1–27.
[58] Di Sieno L, Dalla Mora A, Torricelli A, Maffeis G, Ruggeri A, Tisa S, Tosi A, Conca E, Flocke A, Pifferi A, Taroni P. First in-vivo diffuse optics application of a time-domain multiwavelength wearable optode. In: Biophotonics congress: biomedical optics 2022 (Translational, Microscopy, OCT, OTS, Brain). Optica Publishing Group; 2022. OTu4D.3.